Accelerated Cardiovascular Magnetic Resonance Imaging Using Radial Acquisition with Compressed Sensing

Citation

Nam, Seung Hoon. 2012. Accelerated Cardiovascular Magnetic Resonance Imaging Using Radial Acquisition with Compressed Sensing. Doctoral dissertation, Harvard University.

Thesis advisor | Author

Vahid Tarokh | **Seung Hoon Nam**

Accelerated Cardiovascular Magnetic Resonance Imaging Using Radial Acquisition with Compressed Sensing

Abstract

Magnetic resonance imaging (MRI) is a medical imaging technique that can visualize internal organs for examination and diagnosis. It is non-invasive and ionizing radiation-free, and provides good contrast between different soft tissues. One of the drawbacks of MRI is its lengthy acquisition time. Significant research has been done in order to accelerate the MRI data acquisition and reduce the scan time. Compressed sensing (CS) has been recently proposed for accelerating MRI acquisition time. Compressed sensing recovers the desired image from undersampled MRI dataset by exploiting the sparsity of MR image in transform domain. In this thesis, we propose CS reconstruction methods in various cardiovascular MRI applications for accelerated imaging.

We consider 3D whole-heart coronary MRI. Isotropic 3D radial trajectories allow undersampling of k-space in all three dimensions, enabling accelerated acquisition of volumetric data. Our CS based approach provides further acceleration by removing undersampling artifacts and improving image quality. However, the underlying heavy computational overhead of this method is also a limiting factor which depreciates the applicability of CS. A parallelized implementation of an iterative CS reconstruction for 3D radial acquisitions using a graphics processing unit is presented to reduce the reconstruction time.

The efficacy of CS is also investigated in cardiac cine MRI. Cardiac function is usually assessed using segmented cine acquisition with multiple breath-holds (BHs). Subjects are given resting periods between adjacent BHs, where no data is acquired, resulting in low acquisition efficiency. We propose an accelerated radial acquisition for BH cine imaging which utilizes the resting period to acquire additional free-breathing (FB) data without increasing scan time. The difference image between BH and FB acquisitions is used as the sparsity regularization of the CS reconstruction.

Compressed sensing can be used as a respiratory motion correction technique in FB whole-heart MRI. Respiratory motion causes aliasing artifacts and blurring on the resulting image. To obtain motion-free images, a respiratory navigator is often used to track the heart position, but the scan efficiency is reduced to 30-50% resulting in a prolonged scan. We propose a CS reconstruction to correct respiratory motion by using an undersampled dataset which only contains motion-free k-space lines whereas the motion-corrupted lines are excluded from the reconstruction.

Contents

List of Figures

List of Tables

Citations to Previously Published Work

Most of the Chapters of this thesis have appeared in print or submitted for publication elsewhere. Below is a list, by Chapter number.

- Chapter 2 and 3: "Compressed Sensing Reconstruction for Whole-Heart Imaging with 3D Radial Trajectories: A Graphics Processing Unit Implementation," S. Nam, M. Akçakaya, T. Basha, C. Stehning, W. J. Manning, V. Tarokh and R. Nezafat, *Magnetic Resonance in Medicine*, March 5, 2012.

- Chapter 2 and 3: "A GPU Implementation of Compressed Sensing Reconstruction of 3D Radial (Kooshball) Acquisition for High-Resolution Cardiac MRI," S. Nam, T. Basha, M. Akçakaya, C. Stehning, W. J. Manning, V. Tarokh and R. Nezafat, *Proceedings 19th Scientific Meeting, International Society for Magnetic Resonance in Medicine*, Montreal, Quebec, 2011.

- Chapter 4: "Compressed Sensing Reconstruction for Undersampled Breath-Hold Radial Cine Imaging with Auxiliary Free-Breathing Data," S. Nam, S. N. Hong, M. Akçakaya, Y. Kwak, B. Goddu, K. V. Kissinger, W. J. Manning, V. Tarokh and R. Nezafat, *submitted for publication in Magnetic Resonance in Medicine*, March, 2012.

- Chapter 4: "Improved Accelerated Breath-hold Radial Cine Image Reconstruction by Acquiring Additional Free-Breathing Data between Breath-holds," S. Nam, M. Akçakaya, Y. Kwak, B. Goddu, K. V. Kissinger, W. J. Manning, V. Tarokh and R. Nezafat, *Proceedings 15th Annual Scientific Sessions, Society for Cardiovascular Magnetic Resonance*, Orlando, FL, 2012.

Acknowledgments

First of all, I would like to thank my advisor Prof. Vahid Tarokh who gave me all the support, inspiration and feedback for my research. He guided me with a lot of patience and encouragement. I feel really honored to have Vahid as my Ph. D. advisor. I would also like to thank Vahid for having introduced me to Prof. Reza Nezafat, my co-advisor at Beth Israel Deaconess Medical Center. Reza taught me how to perform research independently and how to work as a team. When I went into a slump with my research in the middle of my Ph. D. program, he encouraged me a lot and stimulated me with patience so that I can recover quickly. I feel extremely lucky to have had him as my advisor.

I would like to thank the members of the SEAS faculty, Prof. Roger Brockett, Prof. Yue Lu and Prof. Donhee Ham for their valuable teaching and advice.

I had the pleasure of working with great people in the Tarokh group, Jinsoo Park, Donwoon Bai, Sang Joon Kim, Mehmet Akcakaya and Yongjun Kwak, and all the other members of the lab. My collaborators at BIDMC have been really helpful in creating a friendly and intellectually challenging atmosphere. I would like to thank Mehdi Hedjazi-Moghari, Peng Hu, Tamer Basha, Jaime Shaw, Sebastien Roujol, Kraig Kissinger and Beth Goddu.

I would like to thank all my family members, my father and mother, father and mother in law, brothers and sister. I cannot imagine getting this degree without their endless support, love and prayers. Even though we have been apart for a long time, I can always feel your presence and have always felt we are connected.

Finally and most importantly, I would like to thank my wife Jeeyoon and my two little kids, Grace and Brian. This thesis could have not existed without your infinite support, sacrifice, encouragement and love. You are the reason I'm living.

Dedicated to my father, Jungdo Nam,
and my mother, Haesook Kim.

Chapter 1

Introduction

As the amount of the information is fast increasing in every aspect of human life, there should be a way to deal with the massive amount of the accumulated data. It is very common to compress the data either in lossless or lossy format before it is stored. For example, digital music, pictures and movies can be compressed in MP3, JPEG, and MPEG formats. Compression of data often involves extraction of small but the most important portion of the data in a transform domain, such as Fourier transform, discrete cosine transform (DCT) and wavelet transform, with the assumption that the data can be well represented only using the small fraction to the extent that there happens no or little loss of information. This is called “sparsity” or “compressibility” of the data, and is well-understood and widely used in the data compression of digital images. For example JPEG[1] and JPEG2000[2] utilize DCT and wavelet transform, respectively. Provided the fact that most of the signals have compressibility to some degree, it would be even better if we can directly acquire the important information from the signal and not acquire the entire signal at the time of measurement/acquisition. Not to mention that the compression saves the cost of storage, it will also reduce the cost of acquiring the data as it is often the case that data acquisition is time consuming. This is the basic idea of “Compressed Sensing” or “Compressive Sampling”. Medical images are compressible as well. Especially the magnetic resonance imaging requires long scan time and therefore will benefit from acquiring the compressed information directly from a small number samples at the time of measurement. This will reduce the acquisition time, improve the scanner throughput and ease the patient cooperation. It has been shown that if the underlying image has transform sparsity, and if the measurements result in incoherent artifacts in that transform domain, then the image can be properly reconstructed from the small number of measurements by using appropriate signal processing methods which could include nonlinear operations.

In the remainder of this chapter, we will first provide the appropriate background in compressed sensing (CS) and related mathematical theories. Then we will provide the outline of the remainder of this thesis, and conclude this chapter with the summary of the contributions of this thesis.

1.1 Compressed Sensing

Suppose we are dealing with a linear system with a input signal $\mathbf{x} \in \mathbb{C}^M$ where $\mathbb{C}$ denotes the complex field, an acquisition (or an encoding) matrix $\mathbf{A} \in \mathbb{C}^{N \times M}$, and a measurement vector $\mathbf{y} \in \mathbb{C}^N$ from the acquisition equation $\mathbf{y} = \mathbf{A}\mathbf{x}$. Our goal is to estimate the input vector $\mathbf{x}$ from the measurement vector $\mathbf{y}$. If the number of measurements is equal to the number of unknown variable, i.e., $M = N$, the problem can be solved, for a non-singular matrix $\mathbf{A}$, by multiplying the inverse matrix of $\mathbf{A}$ to the measurement vector, $\hat{\mathbf{x}} = \mathbf{A}^{-1}\mathbf{y}$. If $M < N$, the system is called over-determined and there may or may not exist a solution depending on the specific system. If there does not exist an exact solution, it is often desirable to find a solution in least-squares sense, i.e., minimizing $||\mathbf{y} - \mathbf{A}\mathbf{x}||_2^2$, where the l_p norm is defined as

$$||\mathbf{s}||_p = \left(\sum_{i=1}^{n} |s_i|^p \right)^{(1/p)}, p > 0. \tag{1.1}$$

When $M > N$, the system is called under-determined and may have an infinite number of solutions. We need to introduce more constraint on the system in such a way that solving the linear system gives us the most sensible solution. Usually a priori information about the input vector $\mathbf{x}$ is often used to constrain the solution. In the next section, we will provide more details of this problem and the conditions under which this problem can be efficiently solved.

1.1.1 Sparsity in Transform Domain

We note that the formulation described in this section is abstract and general, but it is based on a specific assumption that is known to be valid in various settings in image and signal processing areas. Supposed the object we are interested in is a vector $\mathbf{x} \in \mathbb{C}^M$, which can either be an image or a signal with total M pixels or samples. Suppose there also exists an orthonormal basis (ψ_i, $i = 1, 2, \cdots, M$) for $\mathbb{C}^M$, for example, a Fourier basis or a wavelet basis, depending on the specific application and the property of the object of interest. The transform domain coefficients $\theta = (\theta_1, \theta_2, \cdots, \theta_M)^T \in \mathbb{C}^M$, $\theta_i = \langle x, \psi_i \rangle$ of the input signal are assumed to be sparse in the sense that $||\theta||_0 = |\{\theta_i | \theta_i \neq 0\}| = L$, where $L << M$. In other words, the transform domain representation has L nonzero elements out of total M elements. The l_p norm with some $0 < p < 2$ is also often used instead of the l_0 norm as the measure of sparsity. It has been observed that most of the natural and human-made signals can be made sparse (or compressible) in certain transform domains.

Now we turn our attention to a problem of measuring (or detecting) a signal $\mathbf{x} \in \mathbb{C}^M$. Conventional way of measuring is to directly pick up the value of each coefficient of the M coordinates of the signal vector. This is the case when the acquisition matrix is given as an identity matrix, $\mathbf{A} = \mathbf{I}$. On the other hand, the measurements may be given as different linear combinations of all the M samples in $\mathbf{x}$. After the sampling is over, the measured signal may undergo a compression stage before it is stored or transmitted to elsewhere, so some of the non-significant coefficients are discarded during the compression. Now a fundamental question arises: if x is an unknown signal whose transform domain representation θ satisfies the sparsity constraint $||\theta||_0 = L$, is it possible to reconstruct the original x from a reduced number $N << M$ of measurements? Can we compressively sample the data so that we can simultaneously perform data compression at the time of acquisition? The answer is “yes” for certain type of acquisition matrices $\mathbf{A}$. For more details, the readers are referred to [3, 4].

Let $\mathbf{\Psi}$ be the sparsifying transform, i.e., $\theta = \mathbf{\Psi}\mathbf{x}$, where the transform domain vector satisfies the sparsity constraint $||\theta||_0 = L$ such that $L << M$. The measurement is performed by taking a linear combination of the coefficients of $\mathbf{x}$ using each column of the $M \times N$ acquisition matrix $\mathbf{A}$. Thus the measurement vector $\mathbf{y}$ is given by $\mathbf{y} = \mathbf{A}\mathbf{x}$, where $L \leq N << M$. The number of measurements is less than the number of coefficients in $\mathbf{x}$ but greater than or equal to the number of nonzero coefficients in

$\mathbf{\Psi}$.

1.1.2 Reconstruction

The problem of reconstructing the original signal can be expressed as

$$\arg\min_{\theta} ||\theta||_0 \quad \text{s.t.} \quad \mathbf{y} = \mathbf{A}\mathbf{x},\ \theta = \mathbf{\Psi}\mathbf{x}, \tag{1.2}$$

where $\mathbf{y}$ is an N-dimensional column vector, $\mathbf{A}$ is an $N \times M$ matrix, $\mathbf{\Psi}$ is an $M \times M$ matrix. The final estimate of $\mathbf{x}$ is given by $\hat{\mathbf{x}} = \mathbf{\Psi^{-1}}\theta$. For the remainder of this section, without loss of generality, we will restrict our interest on the identity transform $\mathbf{\Psi} = \mathbf{I}$. Thus the problem is written as

$$\arg\min_{\mathbf{x}} ||\mathbf{x}||_0 \quad \text{s.t.} \quad \mathbf{y} = \mathbf{A}\mathbf{x}. \tag{1.3}$$

Minimization of l_0 norm in Equation (1.2) is a nonconvex optimization problem which is NP-hard [5] and intractable for a large size vector. Solving l_0 norm minimization involves combinatorial search over all possible sparse subset of $\{1, 2, \cdots, M\}$ which satisfies $\mathbf{y} = \mathbf{A}\mathbf{x}$. Fortunately, it has been shown that solving l_1 minimization problem instead of solving l_0 minimization gives a near-optimal solution and sometimes exactly produces the same solution as the l_0 minimization for given conditions [3, 6, 7]. We will briefly review the l_1 minimization problem in the following.

There has been extensive research on the equivalence of l_0 and l_1 minimization [8, 9, 10, 11, 12], and also research on the l_1 minimization approaches in the CS literature [3, 6, 13, 14, 15, 16, 17, 18, 19, 20]. The l_1 minimization problem can be expressed as

$$\arg\min_{\mathbf{x}} ||\mathbf{x}||_1 \quad \text{s. t.} \quad \mathbf{y} = \mathbf{A}\mathbf{x}, \tag{1.4}$$

where we restricted our interest to identity transform as the sparsifying transform again. In the paper by Candes and Tao [6], the authors introduced a concept known as *restricted isometry property* (RIP) to prove many theorems of CS and to explain the conditions under which CS can successfully reconstruct the signals. RIP characterizes matrices which are nearly orthogonal when operating on sparse vectors. To make a quantitative measure on this property, the following definition is introduced.

Definition 1.1.1. *(Restricted Isometry Constants [6]): For every integer* $1 \leq S \leq N$*, we define the* S*-restricted isometry constants* δ_S *to be the smallest quantity such that* $\mathbf{A}_\Omega$ *obeys*

$$(1-\delta_S)||\mathbf{c}||_2^2 \leq ||\mathbf{A}_\Omega \mathbf{c}||_2^2 \leq (1+\delta_S)||\mathbf{c}||_2^2,$$

for all subsets Ω *of cardinality at most* S *and all real coefficients* $\mathbf{c} \in \mathbb{R}^{|\Omega|}$.

where $\mathbf{A}_\Omega$ is defined as the matrix whose columns are selected as the subset of the columns of $\mathbf{A}$, i.e., $\mathbf{A}_\Omega$ is the collection of the column vectors $\{\mathbf{a}_j \, : \, j \in \Omega\}$, where $\mathbf{a}_i$ denotes the i^{th} column of $\mathbf{A}$.

It can be proved that by using this property, if $\mathbf{A}$ satisfies the RIP with $\delta_S + \delta_{2S} + \delta_{3S} < 1$ and $||\mathbf{x}||_0 = L \leq S$, then the l_1 minimization problem will provide the same solution as the l_0 minimization problem [6]. The question now is: Which matrices satisfy the RIP for the least possible range of N? It is known that random matrices constructed using random entries from certain probability distribution yield the RIP with high probability. For a fixed value of δ_S, the tightest range possible is $N > C_{\text{RIP}} L \log(M/L)$ with overwhelming probability for all large N, when the elements of $\mathbf{A}$ are drawn from an independent and identically distributed (i.i.d.) Gaussian random variable with mean 0 and variance $\frac{1}{N}$.

The problem of more practical interest is when the measurement is not perfect and some additive noise is introduced, or when $\mathbf{x}$ is not strictly sparse in the transform domain but can be well approximated by its largest L coefficients. In either of the cases, the measurement vector can be expressed as

$$\mathbf{y} = \mathbf{A}\mathbf{x} + \mathbf{n}.$$

This is referred to as *noisy compressed sensing* problem. When the noise signal is bounded, there exists a theory determining the accuracy of the reconstruction method that solves the following convex problem

$$\arg\min_{\mathbf{x}} ||\mathbf{x}||_1 \quad \text{s.t.} \quad ||\mathbf{y} - \mathbf{A}\mathbf{x}||_2 \leq \epsilon, \tag{1.5}$$

where $\epsilon > ||\mathbf{n}||_2$ is a nonnegative scalar which characterizes the noise level and the fidelity of the measurement to the original signal. Suppose $\hat{\mathbf{x}}$ is a solution to Equation (1.5), then it is proved that the solution satisfies

$$||\mathbf{x} - \hat{\mathbf{x}}||_2 \leq c_1 ||\mathbf{n}||_2 + c_2 \frac{||\mathbf{x}^{(L)} - \mathbf{x}||_1}{\sqrt{L}}, \tag{1.6}$$

where $\mathbf{x}^{(L)}$ denotes the truncated approximation corresponding to the L largest values of $\mathbf{x}$ (in absolute value), and c_1 and c_2 are constants [4, 13].

Let us go back to the original problem where the input signal is sparse in another transform domain rather than the identity transform. We also assume that the acquisition matrix is given as a subset $\Omega \in \{1, 2, \cdots, M\}$ of column vectors of the Fourier encoding matrix $\mathbf{F}$, $\mathbf{A} = \mathbf{F}_\Omega$ where $\mathbf{F}_\Omega$ is the $N \times M$ matrix consisting of the rows of $\mathbf{F}$ indexed by Ω. This setting describes the case of the undersampled magnetic resonance imaging acquisition we are going to discuss in this thesis. Then the goal is to search for the coefficients in the $\mathbf{\Psi}$ domain with minimum l_1 norm that match to the measurement in domain $\mathbf{A}$. Then the *mutual coherence* of $\mathbf{A}$ and $\mathbf{\Psi}$ is defined as [21]

$$\mu(\mathbf{A\Psi}) = \max_{i,j} |(\mathbf{A\Psi})_{ij}|. \tag{1.7}$$

Given a fixed value of mutual coherence, it is shown that l_1 minimization problem with equality constraint can be solved when $N > C_{\mathrm{I}}\mu^2(\mathbf{A\Psi})L\log(M)$ [21]. We note that the minimum value of the mutual coherence is 1 and this value is achieved, for example, when $\mathbf{A}$ is a partial Fourier matrix and $\mathbf{\Psi}$ is an identity matrix.

1.2 Outline of Thesis

We have covered the prerequisite knowledge on CS and MRI in this chapter. The rest of this thesis will mainly deal with the application of the CS on undersampled MRI reconstruction, especially in cardiac MRI reconstruction problems. Chapter 2 deals with the CS reconstruction of whole-heart MRI with 3D radial trajectories. Three dimensional MRI acquisition for whole-heart coverage takes long time due to the large coverage and the respiratory and cardiac motion. We seek to accelerate the acquisition of 3D data by using CS reconstruction in conjunction with 3D radial trajectory. 3D radial trajectory has better data acquisition efficiency compared with standard Cartesian trajectory with true isotropic resolution and better motion property, but the reconstruction of radial trajectory is not as straightforward as that of Cartesian. An iterative CS reconstruction method is implemented and the performances of different sparsifying transforms, i.e., identity transform and wavelet transform are evaluated.

In Chapter 3, the iterative CS reconstruction method for undersampled 3D radial trajectory described in Chapter 2 is implemented using the graphic processing unit (GPU). The computational overhead of the iterative reconstruction for 3D trajectory increases as the size of the 3D data increases, and is proportional to the number of iterations. The complexity of the reconstruction of 3D radial trajectory is a lot higher than that of Cartesian trajectory due to gridding and re-gridding operations, resulting in prolonged reconstruction time. Therefore, feasibility of CS for whole-heart 3D radial trajectory for accelerated acquisition has not been studied until recently. GPU implementation with highly parallelized execution of the gridding and re-gridding operations enables faster reconstruction of undersampled radial acquisition. The speedup in the total reconstruction time of the GPU implementation is compared with that of the standard C implementation.

In Chapter 4, we present a novel CS reconstruction method for cine MRI which utilizes a new sparsifying regularization. The clinical workflow of cardiac cine MRI involves multiple breath-hold (BH) acquisitions and resting period of 20-30 seconds between BHs. The resting periods are spent for the patient to recover from the BH without acquiring any MRI data, thus results in substantially low acquisition efficiency. We seek to utilize this resting period to acquire additional auxiliary free-breathing data which will be used to sparsify the cardiac phase images for successful CS reconstruction. The proposed CS reconstruction method and a conventional CS reconstruction method are used to reconstruct the undersampled BH cine acquisitions, and the performances are compared to evaluate the feasibility of the proposed acquisition and CS reconstruction strategy.

In Chapter 5, we propose to use CS reconstruction as a motion correction technique in FB 3D radial acquisition. Respiratory motion causes aliasing artifacts and blurring on the resulting image. Conventionally, a respiratory navigator can be used to monitor the heart position and re-acquire k-space lines if the displacement of heart from the reference position is greater than a predefined value. This results in a reduced scan efficiency and prolongs the scan. Proposed CS reconstruction utilizes a subset of the acquired k-space data which only contains motion-free k-space lines to correct the respiratory motion, whereas the motion-corrupted lines are excluded from the reconstruction.

1.3 Summary of Contributions of This Thesis

In Chapter 2, the CS reconstruction is first implemented for high resolution 3D radial whole-heart MRI. The scan of the large volumetric whole-heart image with high spatial resolution requires lengthy acquisition time, which causes low scan throughput, high cost and patient inconvenience. The CS reconstruction provides improved image quality for highly undersampled 3D radial trajectory, resulting in reduced scan time by a factor of 2 to 3 compared to the conventional gridding reconstruction.

In Chapter 3, the CS reconstruction for 3D radial trajectory proposed in Chapter 2 is implemented using GPU programming. The gridding and re-gridding operations in the reconstruction procedure are of high complexity especially for large size 3D acquisitions, preventing the practical use of CS reconstruction. The GPU implementation provides up to 54 times speed-up in the reconstruction time compared with the standard C++ implementation. The GPU implementation accelerates the CS reconstruction enabling the feasibility of CS reconstruction and accelerated acquisition for 3D radial whole-heart imaging.

In Chapter 4, novel accelerated acquisition and CS reconstruction for radial cine MRI are proposed with the use of new sparsifying regularization. The use of difference images between the BH and FB images as the sparsifying regularization is first proposed in this thesis, and it generates sparse images without using other sparsifying transform such as wavelet or finite difference. Acquiring additional FB images during the resting period without increasing the total scan time is also first proposed in this thesis. The proposed accelerated acquisition and CS reconstruction allow similar image quality with fully-sampled images for a sampling density of 33%, enabling reduced scan time by a factor of 3.

In Chapter 5, a motion correction technique using CS reconstruction for free-breathing 3D radial whole-heart MRI is proposed. The proposed motion correction recovers motion-free images by the CS reconstruction using the undersampled k-space data which only contains motion-free k-space lines. The proposed method retrospectively discards the motion-corrupted k-space lines without re-acquiring them, thus it provides a fixed scan time and an improved scan efficiency compared with prospectively navigator-gated acquisition.

Chapter 2

Compressed Sensing Reconstruction for Whole-Heart Imaging with 3D Radial Trajectories

Cardiac MR (CMR) data acquisition is usually performed using two-dimensional (2D) multi-slice acquisition. Imaging using a single large 3D slab covering from the base to the apex of the heart can significantly simplify image prescription. Whole-heart coronary MRI, analogous to coronary multi-detector CT, has replaced multiple small-slab targeted acquisitions for the individual coronary arteries [22, 23, 24]. A single breath-hold accelerated 3D cine scan has been previously investigated for evaluation of cardiac function [25, 26, 27]. Free-breathing, 3D late Gadolinium enhancement (LGE) imaging has been used to identify fibrosis/scar with improved spatial resolution or coverage [28, 29]. Recently, 3D perfusion has also been applied to improve spatial coverage [30, 31]. The advantages of 3D acquisition include superior spatial resolution especially in through plane, ease of image prescription, superior signal-to-noise ratio (SNR) and easy reformatting of the image in any desired plane. However, one major disadvantage of 3D imaging is the long data acquisition time. For coronary MRI, a longer scan time usually makes the scan more susceptible to respiratory motion. For LGE, it results in imaging artifacts due to changes in optimal inversion time as the contrast washes out. For cine and perfusion, it usually results in lower temporal resolution. Therefore, methods to reduce scan time in 3D imaging could significantly improve clinical utilization of 3D CMR.

Three dimensional whole-heart data is commonly acquired using Cartesian k-space sampling scheme, however non-Cartesian samplings, e.g. radial or spiral have better data acquisition efficiency [32, 33]. Both 3D stack of stars and 3D radial (kooshball) with isotropic spatial resolution have been previously used in 3D CMR [32, 34, 35]. In these samplings, a Nyquist sampling is not necessarily needed and an undersampling does not yield distinct fold-over artifacts. Instead the undersampling usually results in streaking artifacts. This allows high undersampling with less pronounced imaging artifacts compared to Cartesian acquisitions at the same sampling density. These potential benefits have been previously exploited to achieve whole-heart coronary MRI with isotropic spatial resolution [36]. It has also been extensively investigated to improve dynamic imaging such as phase contrast, MR angiography and cine imaging [37, 38, 39].

For single-phase anatomical imaging such as coronary MRI, gridding algorithm is commonly used for reconstruction of the 3D radial acquisition [40]. Although the gridding algorithm can efficiently reconstruct data acquired using 3D radial trajectory, its performance deteriorates significantly for highly undersampled data due to significant undersampling of outer k-space region [41]. Parallel imaging methods including SENSE [42] and GRAPPA [43] have been previously applied for 2D radial acquisitions to reduce the streaking artifacts [44, 45]. Recently, compressed sensing (CS) has been applied to remove the streaking artifacts for 2D radial acquisitions [41, 46]. In this approach, additional constraints based on image properties are used to improve the image reconstruction. The CS reconstruction techniques are usually accompanied by iterative procedures to avoid the inversion of large size matrices [47]. Although initial results in 2D have been very promising, there is currently no data on the utility of such a reconstruction for 3D radial CMR acquisition. The computational overhead of the iterative CS reconstruction increases as the size of the 3D k-space increases, and is proportional to the number of iterations that the reconstruction method uses. The heavy computational overhead of the iterative CS reconstruction for 3D radial acquisition results in prolonged reconstruction time, therefore, the feasibility of CS for 3D radial acquisition for accelerating 3D CMR has not been previously demonstrated.

In this chapter, we evaluate the performance of an iterative CS reconstruction for 3D radial acquisition and subsequently investigate the efficacy of 3D radial acquisition with CS reconstruction for whole-heart coronary MRI.

2.1 Materials and Methods

2.1.1 Three Dimensinal Radial Acquisition

A 3D radial sampling trajectory used in this chapter consists of N_i interleaves, where each interleaf has N_p projection lines of N_s sample points [36]. Each interleaf is the rotated version of the first interleaf around the k_z-axis. Figure 2.1 demonstrates the end points of the projection lines in one example interleaf. The normalized readout gradients G_x, G_y and G_z are given as:

$$\begin{aligned} G_z(p) &= \frac{p-0.5}{N_p} - 1, && (2.1)\\ G_x(p,i) &= \cos\phi(p,i) \cdot \sqrt{1-G_z^2(p)}, && (2.2)\\ G_y(p,i) &= \sin\phi(p,i) \cdot \sqrt{1-G_z^2(p)}, && (2.3) \end{aligned}$$

and

$$\phi = \sqrt{\frac{2(N_p-1)\pi}{N_i}} \cdot \sin^{-1}(G_z(p)) + \frac{2i\pi}{N_i} \tag{2.4}$$

where p and i denote the p-th projection of the i-th interleaf for $p = 1, 2, \ldots, N_p$ and $i = 1, 2, \ldots, N_i$. This 3D radial trajectory has highly isotropic coverage of the 3D k-space. The isotropy (or uniformity) of the sampling point distribution can be quantified by the standard deviation of the distance between adjacent sampling points on the k-space sphere, and is kept at less than 10% of the mean distance when the total number of projections $N_p \times N_i$ is between 100 and 10000 [48]. The sampling density of a 3D radial acquisition is defined as the ratio of the total number of k-space samples of the 3D radial acquisition over that of a Nyquist-sampled 3D Cartesian acquisition with the same resolution and the same FOV.

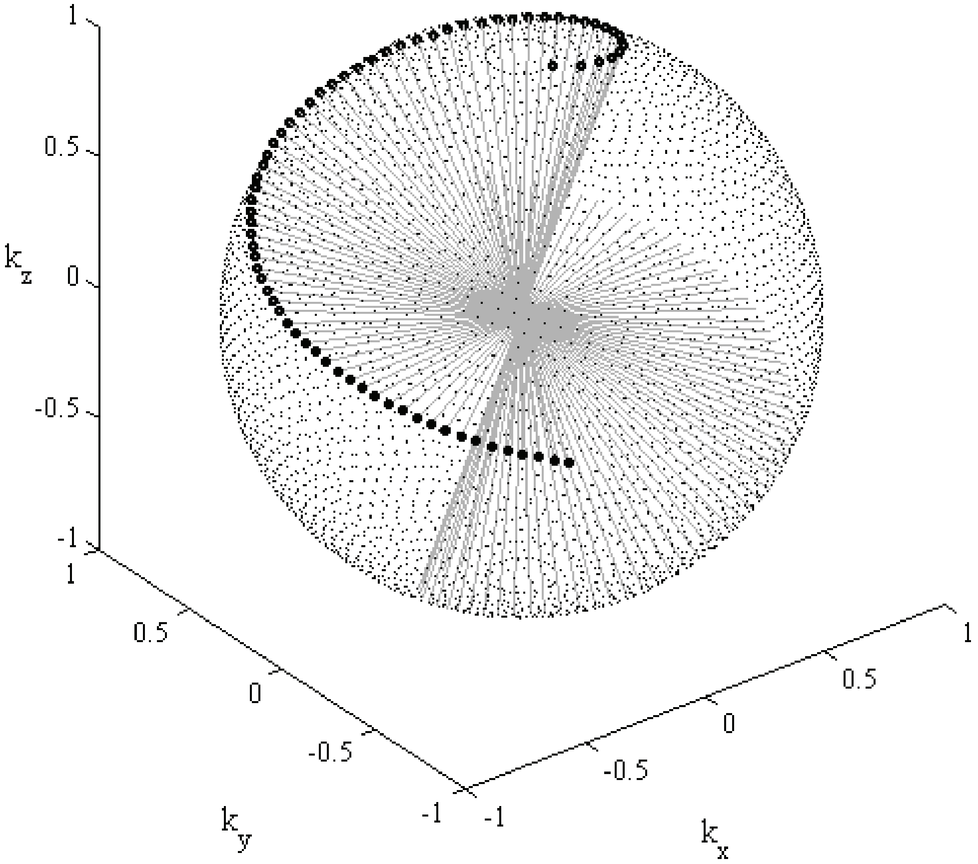

Figure 2.1: 3D radial sampling trajectory. Bold points demonstrate the end points of the projection lines in one example interleaf

2.1.2 Gridding Algorithm for 3D Radial Trajectory

In this chapter, the reconstruction procedure or the conventional gridding algorithm will be briefly reviewed. The gridding algorithm is a simple and efficient implementation of the nonuniform Fast Fourier Transform (NUFFT), and is based on the combination of interpolation of the nonuniform samples to Cartesian grid and the regular FFT. The basic idea of the gridding algorithm is illustrated in Figure 2.2. A 2D example is shown for illustrative purpose, but expansion to 3D gridding is straightforward. Each data point of the non-Cartesian trajectory is convolved with a gridding kernel and the result is re-sampled and accumulated on the Cartesian grid. Once the convolution interpolation is performed for all the data points, a 3D inverse Fourier transform is performed to generate the reconstructed 3D image.

The gridding algorithm can be described in mathematical expressions. The non-Cartesian sampling function $U(k_x, k_y, k_z)$ is given as:

$$U(k_x, k_y, k_z) = \sum_{n=1}^{N} \delta(k_x - k_{x,n}, k_y - k_{y,n}, k_z - k_{z,n}), \tag{2.5}$$

where $k_{x,n}, k_{y,n}$ and $k_{z,n}$ denote the n-th sampling point of the radial trajectory. The acquired data is then $M(k_x, k_y, k_z)U(k_x, k_y, k_z)$, where $M(k_x, k_y, k_z)$ is the actual continuous k-space of the imaging object. Interpolation of the radial sample points using a gridding kernel $S(k_x, k_y, k_z)$ is expressed as

$$\hat{M}(k_x, k_y, k_z) = [(M(k_x, k_y, k_z)U(k_x, k_y, k_z)) * S(k_x, k_y, k_z)] \times \mathrm{III}\left(\frac{k_x}{\Delta k_x}, \frac{k_y}{\Delta k_y}, \frac{k_z}{\Delta k_z}\right), \tag{2.6}$$

where $\mathrm{III}(\cdot)$ is the sampling fuction on the Cartesian grid. Equation (2.6) can be

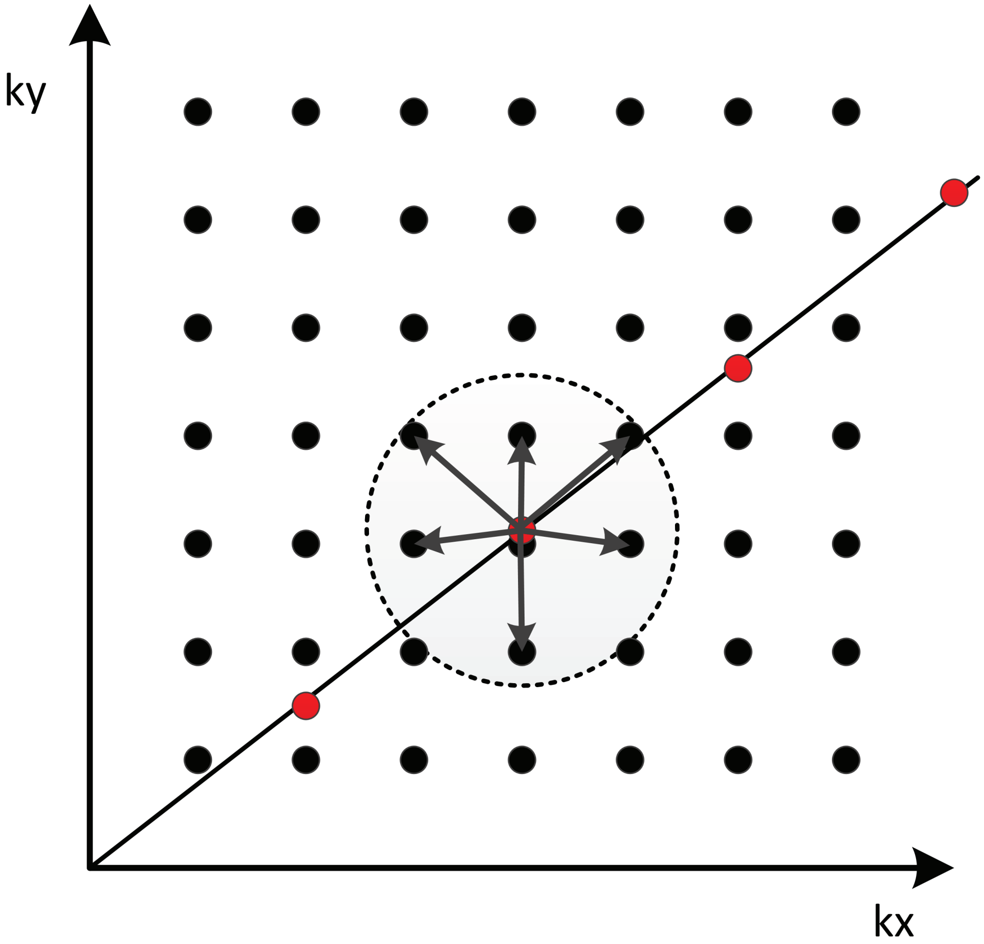

Figure 2.2: Basic idea of gridding algorithm. The radial sample points appear as red dots. Each data point is convolved with a gridding kernel (the dashed circle denotes the gridding kernel size) and the result is re-sampled on the Cartesian grid point.

re-expressed in image domain after the Fourier transform as

$$\hat{m}(x,y,z) = [(m(x,y,z) * u(x,y,z))s(x,y,z)] * \mathrm{III}\left(\frac{x}{FOV_x}, \frac{y}{FOV_y}, \frac{z}{FOV_z}\right). \tag{2.7}$$

In Equation (2.7), the actual image $m(x,y,z)$ is first blurred by the convolution with the transformed sampling function, and then multiplied by the apodization function $s(x,y,z)$ of the convolution kernel. The ideal apodization function will be a rectangular function, but the corresponding convolution kernel in this case is a sinc function which is infinite in extent. A Kaiser-Bessel function is widely used as a good trade-off between the kernel size and ability to suppress the aliasing folding back from the side lobes:

$$S(k) = \frac{1}{L} I_0[B(1-(2u/L)^2)^{1/2}], \tag{2.8}$$

where I_o is the zero-order modified Bessel function of the first kind and B and L are constants. The inverse FFT is given by,

$$s(x) = \frac{\sin(\pi^2 L^2 x^2 - B^2)^{1/2}}{(\pi^2 L^2 x^2 - B^2)^{1/2}}. \tag{2.9}$$

To compensate for the apodization function, de-apodization can be performed in the image domain,

$$\hat{m}(x,y,z) = \frac{1}{s(x,y,z)}[(m(x,y,z) * u(x,y,z))s(x,y,z)] * \mathrm{III}\left(\frac{x}{FOV_x}, \frac{y}{FOV_y}, \frac{z}{FOV_z}\right). \tag{2.10}$$

In Equation (2.10), it is important to mitigate the effect of the sampling function $u(x,y,z)$ for a successful gridding reconstruction. Unlike the Cartesian grid where the data points are uniformly distributed through k-space, the data points of the radial trajectory are distributed more densely at the center of k-space and less at the edges. Each data point is weighted by the inverse of the sampling density before the interpolation in order to compensate for the nonuniform sampling density $\rho(k_x, k_y, k_z)$. This is essential to get an accurate interpolation and to minimize the reconstruction error resulting from uneven weighting of k-space. The k-space estimate after the density compensation is given as

$$\hat{M}(k_x, k_y, k_z) = [(M(k_x, k_y, k_z)\frac{U(k_x, k_y, k_z)}{\rho(k_x, k_y, k_z)} * S(k_x, k_y, k_z)] \times \mathrm{III}\left(\frac{k_x}{\Delta k_x}, \frac{k_y}{\Delta k_y}, \frac{k_z}{\Delta k_z}\right), \tag{2.11}$$

There are different approaches to estimate the sampling density of non-Cartesian trajectories such as geometry-based calculation, numerical approach, and iterative methods, etc [49, 50, 51]. For 3D radial trajectory, the geometry-based calculation provides a sampling density function which is inversely proportional to the square of the radius from the k-space origin. However, for heavily undersampled radial trajectory, the simple geometry-based method fails and more sophisticated method is required.

Since all of the operations in the gridding algorithm are linear, this procedure can be expressed in a matrix-vector format:

$$\hat{\mathbf{x}} = \mathbf{D}\mathbf{F}^*\mathbf{S}\mathbf{P}\mathbf{y}, \tag{2.12}$$

where $\hat{\mathbf{x}}$ is the reconstructed image, $\mathbf{y}$ is the measured 3D kooshball k-space data, $\mathbf{P}$ is a diagonal matrix performing the density compensation, $\mathbf{S}$ denotes convolution matrix, $\mathbf{F}^*$ denotes the inverse Fourier transform, and $\mathbf{D}$ is a diagonal matrix performing the de-apodization.

2.1.3 CS Reconstruction for Undersampled 3D Radial Trajectory

Although the gridding algorithm can efficiently reconstruct an MR image from a 3D radial trajectory, its performance deteriorates significantly for highly undersampled k-space data. Geometry-based DCFs [52, 53] introduce errors in the reconstructed image for undersampled data. An iterative method to estimate the DCF [49, 50, 51] is proposed which makes no assumption that the data satisfy the Nyquist criteria, and provides improved reconstruction for undersampled data. As the sampling density decreases (higher undersampling), however, the kooshball acquisition will present streak-like artifacts in the reconstruction images no matter which DCF is used. The gridding algorithm does not successfully reconstruct the image regardless of the DCF when the data does not satisfy the Nyquist criterion because Equation (2.12) becomes a poor approximation of the actual image. As an alternative approach, the acquired k-space signals can be formulated in an encoding matrix format as $\mathbf{y} = \mathbf{A}\mathbf{x}$, where $\mathbf{A}$ denotes the encoding matrix and $\mathbf{x}$ denotes the actual image. We note that all the voxels of the 3D image are represented in a single column vector $\mathbf{x}$ for mathematical convenience. $\mathbf{A}$ can be considered as taking the reverse steps of the conventional gridding algorithm without the density compensation:

$$\mathbf{y} = \mathbf{A}\mathbf{x} = \mathbf{S}^*\mathbf{F}\mathbf{D}\mathbf{x}, \tag{2.13}$$

where $\mathbf{D}$ is a diagonal matrix performing the de-apodization, $\mathbf{F}$ denotes the fast Fourier transform (FFT) matrix, and $\mathbf{S}^*$ denotes convolution matrix from Cartesian to radial sample points. $\mathbf{x}$ is de-apodized and Fourier transformed into the k-space, then the Cartesian k-space samples are re-gridded onto the 3D radial sample points using the gridding kernel. Unlike the conventional gridding algorithm, it is important to note that the density compensation is not required before the re-gridding because the density of the Cartesian grid is uniform [53]. Equation (2.13) holds regardless of the Nyquist criterion, but the encoding matrix is not invertible for undersampled data, since Equation (2.13) is underdetermined, and there are more than one solution that satisfy the system equation. CS reconstruction utilizes the sparsity of the image to reconstruct the undersampled data using a constrained minimization problem:

$$\arg\min_{\mathbf{x}} \frac{1}{2}||\mathbf{A}\mathbf{x} - \mathbf{y}||_2^2 + \lambda||\mathbf{\Psi}\mathbf{x}||_1, \tag{2.14}$$

where λ is a regularization parameter which determines the tradeoff between the data consistency and the sparsity level of the image, and $\mathbf{\Psi}$ is a sparsifying transform matrix such as wavelet transform or total variation (TV) operator.

To solve Equation (2.14), we adopt an iterative method which alternately enforces the data consistency and sparsity of the image estimate at each iteration [54]. The image update at the $(t + 1)$-th iteration is given by solving the following two sub-problems:

$$\mathbf{u}^t = \mathbf{x}^t + \frac{1}{\alpha_t}\mathbf{A}^*(\mathbf{y} - \mathbf{A}\mathbf{x}^t), \tag{2.15}$$

and

$$\mathbf{x}^{t+1} = \arg\min_{\mathbf{x}} \frac{1}{2}||\mathbf{x} - \mathbf{u}^t||_2^2 + \frac{\lambda}{\alpha_t}||\mathbf{\Psi}\mathbf{x}||_1. \tag{2.16}$$

Equation (2.15) is called data consistency step as the solution tends to decrease the l_2-norm error between the measured data and the k-space of the image estimate. For any unitary sparsifying transform $\mathbf{\Psi}$, Equation (2.16) can be re-expressed with respect to the transform domain vector $\mathbf{z}^t = \mathbf{\Psi}\mathbf{x}^t$ as

$$\begin{aligned} \mathbf{z}^{t+1} &= \arg\min_{\mathbf{z}} \frac{1}{2}||\mathbf{\Psi}^*\mathbf{z} - \mathbf{u}^t||_2^2 + \frac{\lambda}{\alpha_t}||\mathbf{z}||_1 \\ &= \arg\min_{\mathbf{z}} \frac{1}{2}||\mathbf{z} - \mathbf{\Psi}\mathbf{u}^t||_2^2 + \frac{\lambda}{\alpha_t}||\mathbf{z}||_1 \end{aligned} \tag{2.17}$$

Equation (2.17) can be solved by a simple coefficient-wise thresholding function as:

$$z_i^{t+1} = \frac{w_i^t}{|w_i^t|}\max(|w_i^t| - \frac{\lambda}{\alpha_t}, 0), \tag{2.18}$$

where z_i^{t+1} and w_i^t denote the i-th coefficient of the transform domain vector $\mathbf{z}^t$ and $\mathbf{w}^t = \mathbf{\Psi}\mathbf{u}^t$ of the solution of the first sub problem in Equation (2.15), respectively. The second sub problem is called the *thresholding step*. For α_t, we adopt the step size from [55], where α_t is determined so that $\alpha_t\mathbf{I}$ approximates the Hessian of the data consistency term $\nabla^2||\mathbf{A}\mathbf{x}^t - \mathbf{y}||_2^2$ as below:

$$\alpha_t = \frac{||\mathbf{A}\mathbf{x}^t - \mathbf{A}\mathbf{x}^{t-1}||_2^2}{||\mathbf{x}^t - \mathbf{x}^{t-1}||_2^2}. \tag{2.19}$$

The overall iterative reconstruction procedure is summarized in Figure 2.3. The reconstruction starts from an initial image estimate, which in our experiments, was chosen to be the gridding reconstruction. The image is de-apodized, Fourier transformed into k-space, and then re-gridded onto the radial sample points. The estimated radial samples are subtracted from the actual measurement data, convolved

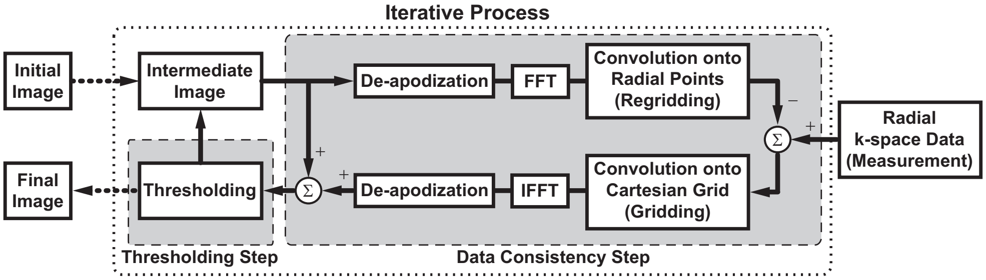

Figure 2.3: 3D radial reconstruction using compressed sensing. The iterative process consists of two steps of data consistency and thresholding. The image is updated to reduce the l_2-norm error between the measured data and the k-space of the image estimate in the data consistency step, and to enforce the sparsity of the image estimate in the thresholding step. The final image is obtained as the result of the iterative process.

onto Cartesian k-space grid, inverse Fourier transformed and an image estimate is obtained after de-apodization. The image estimate is combined with the intermediate image from the previous iteration. The combined image is then thresholded in the transform domain to produce a new image estimate, and the intermediate image is updated. The final image estimate is obtained as the result of the iterative procedures.

2.1.4 Phantom Study

Two experiments were performed for the phantom study. The first experiment is to demonstrate the capability of improving the reconstruction quality of 3D radial acquisitions using the CS reconstruction method. The second experiment is to investigate the convergence properties of the CS reconstruction method over different numbers of iterations.

For the first experiment, a high resolution phantom was scanned with a steady-state free precession (SSFP) sequence using 3D radial trajectories with $N_s = 344$

and $N_i = 10$ for five different sampling densities 7.5, 10, 20, 30 and 40%, which correspond to the number of projections per interleaf N_p of 221, 289, 576, 896 and 1184 respectively. The scan parameters were TR/TE/$\alpha = 3.90/1.94/60°$, FOV $= 240 \times 240 \times 240\ mm^3$, spatial resolution $= 1.4 \times 1.4 \times 1.4\ mm^3$. The acquired 3D radial data were reconstructed by the iterative CS reconstruction method and the conventional 3D gridding algorithm with density compensation, and the reconstructed images were compared. We used both the identity transform and the Daubechies 4 [56] discrete wavelet transform (DWT) for the sparsity regularization term of the CS reconstruction. The regularization parameter, λ was varied from $0.01||\mathbf{A}^*\mathbf{y}||_\infty$ to $0.1||\mathbf{A}^*\mathbf{y}||_\infty$ as in [55, 57] and manually selected to get the best image qualities; $\lambda = 0.05||\mathbf{A}^*\mathbf{y}||_\infty$ gave satisfactory results for most of the cases with both sparsity regularizations. The DCF for the gridding algorithm was calculated using the iterative procedure proposed in [49]. For both the CS reconstruction and the gridding algorithm, a Kaiser-Bessel function in Equation (2.8) with window size 4.0 was used for the convolution kernel [58].

For the second experiment on convergence properties of the reconstruction algorithm, iterative CS reconstructions with both image and wavelet regularizations were performed on the phantom data set with 7.5% sampling density and the intermediate images were stored for different number of iterations.

2.1.5 Whole-Heart Coronary MRI

Whole-heart coronary MR images were acquired on 9 healthy volunteers (2 male, 26±11 years). 3D free-breathing ECG-triggered SSFP sequences were used for imaging the heart with 3D radial trajectories. A respiratory navigator with 7 mm gating window was used for gating and tracking the respiratory motion [59]. The k-space data acquired within the gating window were accepted, and the k-space data acquired outside the gating window were rejected and re-acquired until acquired within the gating window. Within the 7 mm gating window, the position of the imaging volume was adaptively adjusted using a tracking factor of 0.6. The data sets were acquired with $N_s = 392$ and $N_i = 10$ for various sampling densities: two data sets with 6.8%, 12.1%, 24.2% and 36.3%, seven data sets with 10%, 20%, 30% and 40%. The scan parameters were as follows: TR/TE/ = 3.95/1.97/60°, FOV = $256 \times 256 \times 256\ mm^3$, spatial resolution = $1.3 \times 1.3 \times 1.3\ mm^3$. The nominal scan time for the data set with sampling density of 40% was reported to be 5 minutes 13 seconds assuming 100% navigator gating efficiency. For one volunteer, an additional scan with spatial resolution of $1.0 \times 1.0 \times 1.0\ mm^3$ and sampling density of 40% was acquired. The acquired 3D radial data were reconstructed by the three reconstruction methods (i.e. gridding, CS with image domain regularization and CS with wavelet domain regularization), and the reconstructed image quality was compared. The regularization parameter λ of the iterative CS reconstruction was selected to be $\lambda = 0.05||\mathbf{A}^*\mathbf{y}||_\infty$. The DCF for the gridding algorithm was calculated by the same method used in phantom study and the Kaiser-Bessel function with window size 4.0 was used for the convolution kernel.

The empirical convergence properties of the CS reconstructions were also observed similar to the phantom study. The vessel sharpness and the vessel length of the right coronary artery (RCA) were measured using Soap-Bubble software [60] for quantitative assessment of the CS reconstruction method. The user defines the vessel of interest by drawing points along the vessels path in the 3D recosntructed image, and these points are updated with the center of gravity, representing the vessel centerline. The centerline points are then regridded using cubic spline interpolation and the vessel border detedction is performed. The vessel-border is detected with the Deriche edge-detection filter [61], and the vessel delineation (sharpness) is defined as the average edge value along the entire vessel border [62]. In this chapter, a relative vessel sharpness score is used such that the vessel border sharpness is normalized by the maximum vessel centerline value. The sharpness and the length of the vessels with CS reconstruction were compared with the gridding algorithm using a paired t-test. A value of $P < 0.05$ was considered to be statistically significant.

2.2 Results

2.2.1 Phantom Experiments

Figure 2.4 shows the reconstruction results of an example slice of the 3D radial acquisition using the aforementioned algorithms with different sampling densities of 7.5%, 10%, 20%, 30%, and 40%. At the bottom left of each image, a selected region of the phantom is shown at a larger scale. The normalized mean-squared error (MSE) from the reference image with 100% sampling density is also included at the bottom right of each image, calculated as $MSE = ||\mathbf{x}_{ref} - \mathbf{x}_{under}||_2^2/||\mathbf{x}_{ref}||_2^2$, where $\mathbf{x}_{ref}$ denotes the reference image from 100% sampled k-space data and $\mathbf{x}_{under}$ denotes the reconstructed image from the undersampled k-space data. Both of the CS reconstructions show improved image quality compared with the conventional gridding reconstructions, and the improvement is more distinct with lower sampling densities. The streaking artifacts degrade the image quality of the conventional gridding reconstructions for lower sampling densities (20, 10, and 7.5%), while most of the streaking artifacts are removed on the CS reconstructed images for the same sampling densities. Overall, the CS reconstructions have less visible artifact and improved image homogeneity compared with the conventional gridding reconstructions. In particular, the image domain regularization provides better image quality at sharp edges,

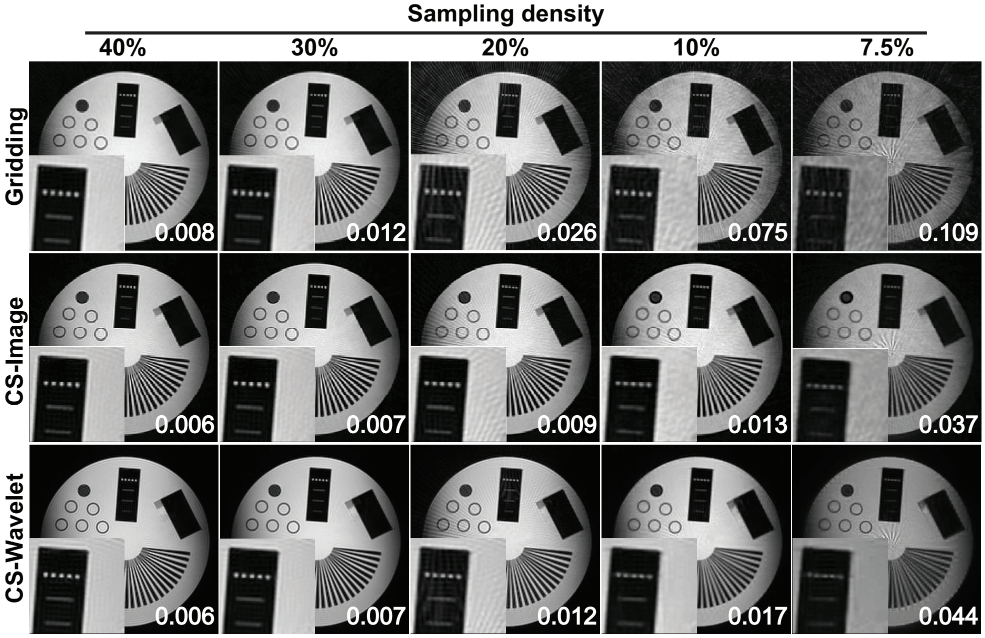

Figure 2.4: Comparison of conventional 3D gridding reconstruction vs. 3D iterative CS reconstruction with different sparsity regularizatuions (image domain and wavelet domain) for a 3D radial acquisition using four different sampling densities (40%, 30%, 20%, 10%, and 7.5%). The number of iterations were 3000 and 500 for CS with image domain sparsity and wavelet domain sparsity, respectively. For high sampling densities all three reconstruction methods yield comparable image quality, For lower densities, both CS CS reconstructions provide superior image qualities compared with the gridding algorithm, while CS with image domain sparsity shows better results at sharp edges and CS with wavelet domain sparsity is better at smooth surfaces. The normalized mean-squared errors are also included at the right bottom of the images.

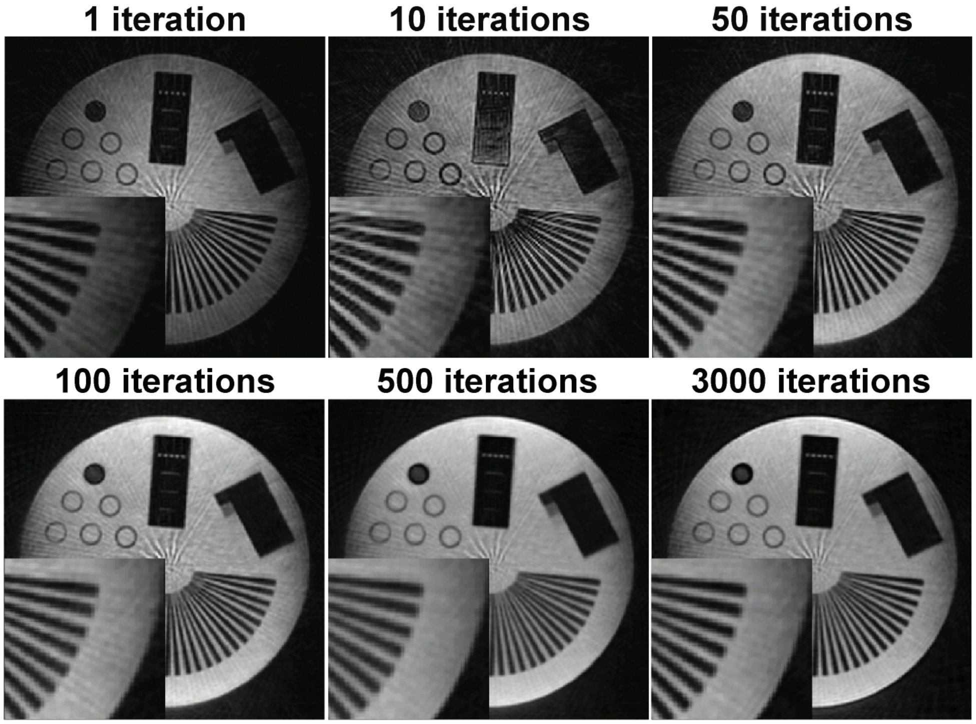

Figure 2.5: CS reconstruction of a phantom imaged with 3D radial with sampling density of 7.5% at different number of iterations, initiated with the conventional gridding reconstruction. The streaking artifacts are gradually removed with some blurring up to 500 iterations, however, with additional iterations the streaking artifacts are suppressed with improved sharpness.

while the wavelet domain regularization is generally better at removing streaking artifacts. The CS reconstruction with image domain regularization provides the least normalized MSE values at all sampling densities.

Figure 2.5 depicts the resulting images generated by the CS reconstruction algorithm for different number of iterations. The streaking artifacts in the earlier iterations are gradually removed as the number of iterations increases, while the image loses the sharpness at the edges of the phantom object and becomes slightly more blurry up to 500 iterations. After additional 2500 iterations the sharpness of the object is improved and the image looks more refined with preserved edges.

2.2.2 In Vivo Experiments

Figure 2.6 and 2.7 show example slices of axial and reformatted sagittal views from 3D whole-heart images with isotropic 1.3 mm spatial resolution reconstructed by conventional 3D gridding reconstruction,as well as the iterative CS reconstruction with image and wavelet domain regularizations for four different sampling densities (6.8, 12.1, 24.2 and 36.3%). The images reconstructed with gridding present streaking artifacts and high-frequency noise-like artifacts, especially at lower sampling densities. Both CS reconstructions were able to substantially suppress these artifacts at lower densities. While the wavelet domain regularization provides cleaner and more homogeneous results in the blood pool, the image domain regularization provides more detailed and sharper edges. The wavelet domain regularization results in checkerboard-like artifacts in the reconstructed image with 6.8% sampling density.

Figure 2.8 illustrates the resulting images of the CS reconstruction with image domain regularization for different number of iterations. The artifacts associated with undersampling are gradually removed and the image quality improves as the number of iteration increases. The blurring of the image during the iterations shown in the phantom (Figure 2.5) was not observed in the in-vivo result. Between 500 and 3000 iterations, there is a slight improvement in the image quality but it was less prominent than the phantom case. Similar trends were observed for the wavelet domain regularized CS reconstruction but no visual improvement was observed after 500 iterations.

Figure 2.9 depicts reformatted RCA images from 3D whole-heart data with spatial resolution of $1.0 \times 1.0 \times 1.0\ mm^3$ and sampling density of 40%, reconstructed by

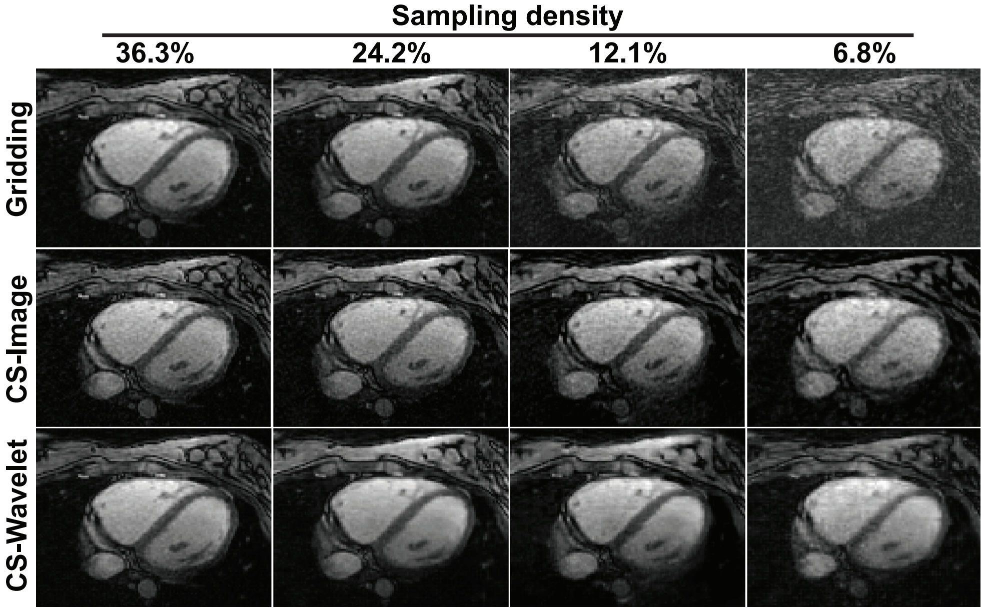

Figure 2.6: Example slices of axial views from 3D whole-heart images reconstructed by conventional 3D gridding reconstruction and iterative CS reconstruction (with 1000 iterations for image domain regularization and 500 iterations for wavelet domain regularization) for different sampling densities. For all the sampling densities, CS reconstructions have less high-frequency streaking artifacts, and the improvement in the image quality is more distinct at lower sampling densities.

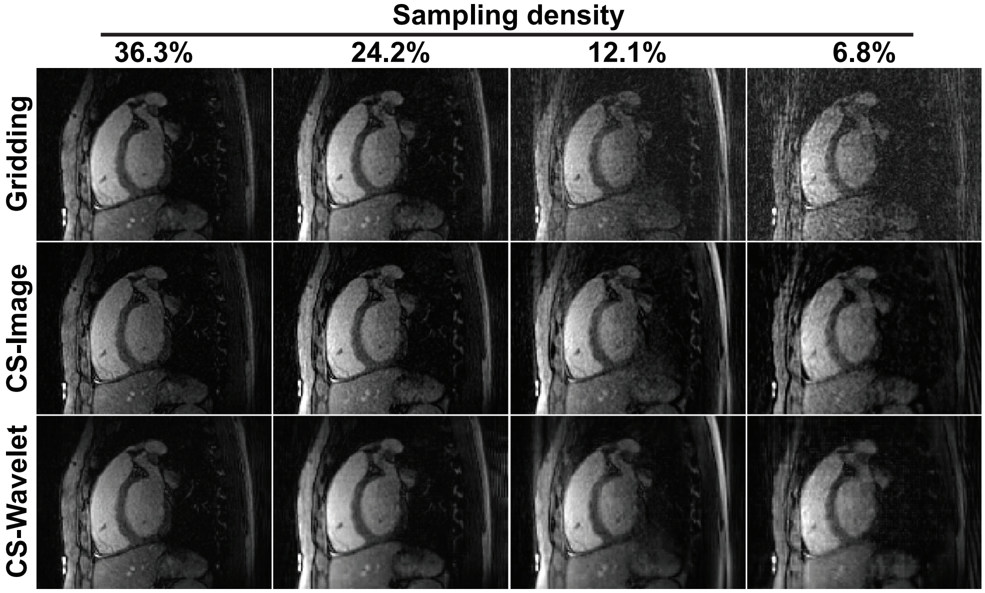

Figure 2.7: Example slices sagittal views from 3D whole-heart images reconstructed by conventional 3D gridding reconstruction and iterative CS reconstruction (with 1000 iterations for image domain regularization and 500 iterations for wavelet domain regularization) for different sampling densities. For all the sampling densities, CS reconstructions have less high-frequency streaking artifacts, and the improvement in the image quality is more distinct at lower sampling densities.

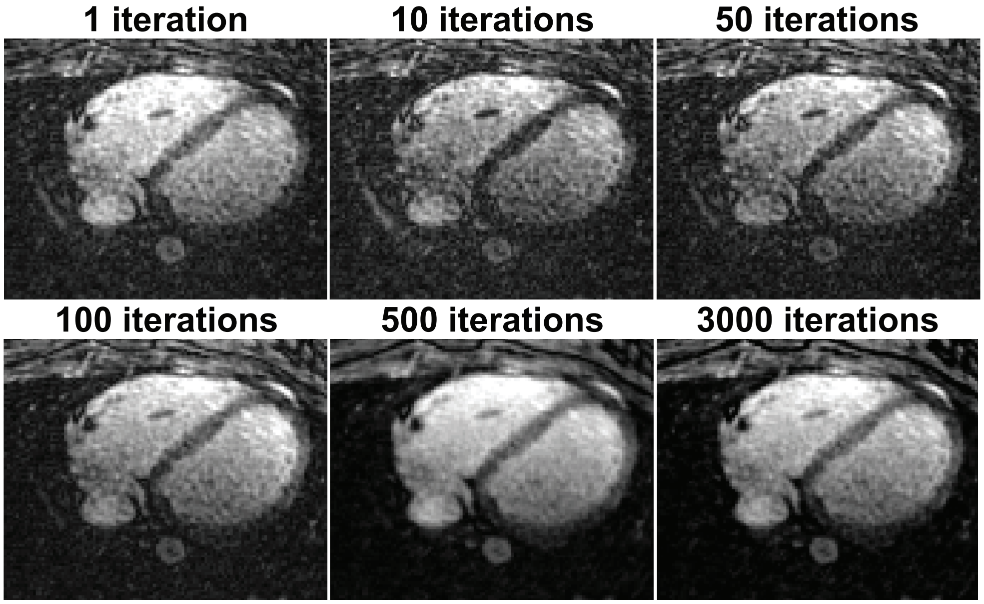

Figure 2.8: An example slice from 3D data-set (sampling density = 6.8%) of the coronary arteries reconstructed using CS with image domain regularization at different iterations. The high-frequency artifacts are gradually removed throughout the iterations up to 500 iterations. Slight improvement was observed after 500 iterations, but it was less prominent that the phantom case (Figure 2.5).

the iterative CS reconstruction with image domain regularization. The data set is retrospectively undersampled to get 10% and 20% sampling densities, and the reconstructed images are shown. Due to the isotropic resolution of the 3D radial acquisition in all three dimensions, the image can be reformatted retrospectively in an arbitrary angle to obtain a desirable imaging plane for visualizing the vessels. Table 2.1 summarizes the quantitative results of the 3D whole-heart images from 6 complete data sets with sampling densities of 10%, 20%, 30% and 40%. The measured vessel lengths increase as the sampling density increases for all the reconstruction methods, but the vessel lengths are not significantly different among the three reconstruction methods. The CS reconstruction with image domain regularization provides higher vessel sharpness for all sampling densities, and the improvements are statistically significant for sampling densities of 10%, 20% and 30% compared with the gridding reconstruction. The CS reconstruction with wavelet domain regularization, however, does not show significant improvement in the vessel sharpness over the gridding reconstruction for any of the sampling densities.

2.3 Discussion

In this chapter, we have evaluated the feasibility of using CS to improve image reconstruction for 3D whole-heart coronary MRI.

The 3D radial trajectory intrinsically has more favorable properties for CS reconstruction. Theoretically, random undersampling of the k-space guarantees a very high degree of incoherence required for CS reconstruction. This is not suitable for MR images since most of the energy is concentrated in a very small area of the center

Sampling density	Reconstruction method	RCA sharpnes	RCA length
10%	CS-Image	$0.65 \pm 0.05^{*,\#}$	7.29 ± 3.02
	CS-Wavelet	0.52 ± 0.06	7.35 ± 2.95
	Gridding	0.53 ± 0.03	6.99 ± 2.82
20%	CS-Image	$0.61 \pm 0.03^{*,\#}$	7.32 ± 4.10
	CS-Wavelet	0.54 ± 0.04	7.08 ± 3.91
	Gridding	0.51 ± 0.04	6.89 ± 3.61
30%	CS-Image	$0.60 \pm 0.05^{*}$	8.41 ± 2.82
	CS-Wavelet	0.54 ± 0.03	8.50 ± 2.76
	Gridding	0.54 ± 0.02	8.52 ± 2.86
40%	CS-Image	0.64 ± 0.04	9.07 ± 3.28
	CS-Wavelet	0.59 ± 0.06	9.13 ± 3.26
	Gridding	0.58 ± 0.05	8.78 ± 3.40

Table 2.1: Mean ± standard deviation of normalized vessel sharpness and vessel length (cm) measured for conventional gridding reconstruction and iterative CS reconstructions. CS reconstruction with image domain regularization improves the vessel sharpness for sampling densities 10%, 20% and 30% compared with the gridding reconstruction. (*: $P < 0.05$ compared with the gridding reconstruction, #: $P < 0.05$ compared with the CS reconstruction with wavelet domain regularization)

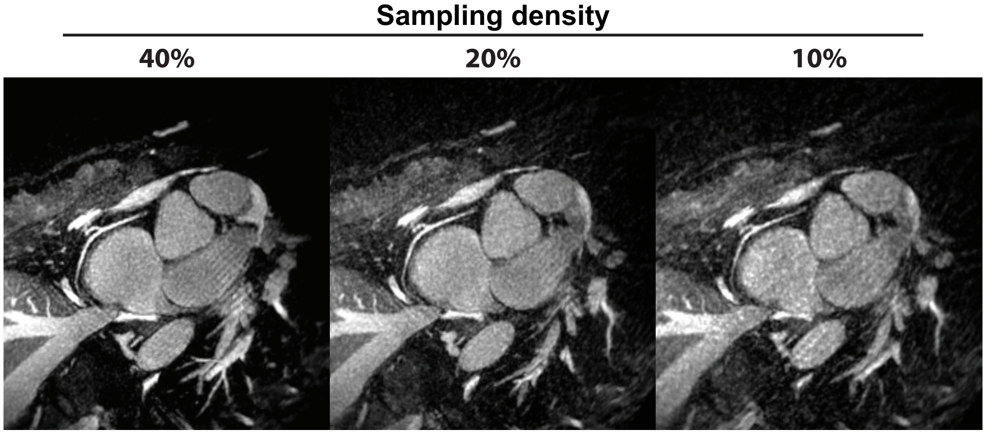

Figure 2.9: Reformatted images of the RCA with isotropic resolution of $(1.0mm)^3$ from whole-heart 3D radial data with three sampling densities (40%, 20% and 10%) by the iterative CS reconstruction with image domain regularization and 1000 iterations. The scan time with sampling density of 40% was 4 minutes 2 seconds assuming 100% navigator gating efficiency. The RCA is clearly visualized with the CS reconstruction for all sampling densities, while slight blurring of the image and residual artifacts are observed at low sampling density (10%).

of k-space, and missing the central k-space lines due to random undersampling may result in reconstruction images of inferior quality. In practice, variable density undersampling is commonly used for Cartesian trajectories. The sampling density varies depending on the radius from k-space center so the center of k-space is fully sampled and the outer region is less sampled (39). The sampling pattern for Cartesian acquisition needs to be carefully designed in order to both have incoherent undersampling artifacts and capture most of the energy of the image. However, each projection line of the 3D radial trajectory always goes through the origin of the k-space and the sampling density is inversely proportional to the radius from the origin of the k-space. Therefore, the inherent sampling property of 3D radial trajectory is suitable for the CS reconstruction and does not require a careful design of undersampling pattern. Moreover, undersampling in all three k-space dimension is also an advantage of the

3D radial trajectory. In Cartesian 3D acquisition, one can only undersample along two k-space directions as undersampling read-out direction does not help to reduce the scan time. The projection lines, i.e. the phase-encode lines, in the 3D radial acquisition, however, are isotropically distributed in the 3D k-space, and one can undersample the k-space lines along arbitrary directions in an isotropic manner. This potentially enables the 3D radial acquisitions to be further undersampled while keeping the incoherent artifact at a comparable level compared to Cartesian acquisitions for CS reconstruction.

3D radial trajectories also provide superior performance with respect to respiratory motion compared to 3D Cartesian trajectories. Oversampling of the central k-space region provides the effect of averaging the low spatial frequency component of the image and thus alleviates the respiratory motion. The aliasing appears as streaking artifact, while the respiratory motion will result in severe ghost images and blurring in the phase-encode direction for Cartesian acquisition. A respiratory navigator with small gating window is widely used to suppress the respiratory motion, but it decreases the scan efficiency and prolongs the scan time if the breathing pattern of the patient significantly changes during the scan. A self-navigated motion correction technique with 3D radial acquisition which incorporates the respiratory navigator into the acquisition was proposed to address this problem [63]. The iterative CS reconstruction can also be incorporated with the motion correction technique enabling the use of highly undersampled 3D radial trajectories to further accelerate the acquisition.

We have utilized the identity transform and the Daubechies 4 wavelets as the sparsifying transforms for the CS reconstruction. The baseline assumption for successful CS reconstruction is that the MR images are sparse in these transform domains. Wavelets have been applied in many MR reconstruction studies [64, 65] but the use of image domain sparsity has been limited to applications such as MR angiography [66, 67]. The 3D radial trajectories are generally oversampled in the read-out direction and this results in an increased FOV larger than the prescribed FOV. The 3D image then contains redundant areas where there is not much signal, making the image sparse in the image domain itself. Both image domain and wavelet domain regularizations have provided improved image quality compared with the conventional gridding algorithm, but exhibited some issues that need to be improved. The CS reconstruction with image domain regularization has a slow convergence speed with the iterative algorithm described in this paper. The CS reconstruction with wavelet domain regularization provides a better convergence speed than the image domain regularization, but shows checkerboard-like and blocky artifacts at low sampling densities. The two step iterative CS reconstruction algorithm used in this paper enables simple and efficient coefficient-wise thresholding for the thresholding step in Equation (2.16) only when the sparsifying transform is given by a unitary matrix. The image domain (identity transform) and Daubechies wavelet transform satisfy this condition, while the well-known and commonly used TV regularization does not. Use of other sparsifying transforms or more advanced techniques that can adaptively capture object-specific sparsity nature [68, 69] can improve the CS reconstruction, which requires further investigation.

2.4 Conclusion

We have implemented an iterative CS reconstruction method for 3D radial acquisitions and evaluated its performance in 3D whole-heart coronary MRI. The CS reconstruction method improves the image quality of highly undersampled 3D radial data sets when compared to the conventional gridding reconstruction, thus enabling higher acceleration and scan time reduction.

Chapter 3

GPU Implementation of the Iterative CS Reconstruction for Undersampled 3D Radial Trajectory

In Chapter 2, we have seen that CS reconstruction enables higher undersampling of 3D radial acquisition compared to the gridding recostruction and this consequently results in reduced scan time. The CS reconstruction techniques are usually implemented with iterative procedures that solve the optimization problem with relatively computationally cheap matrix-vector multiplications [47]. The computational overhead of the iterative CS reconstruction increases as the size of the 3D k-space increases, and is proportional to the number of iterations that the reconstruction method uses. The heavy computational overhead of the iterative CS reconstruction for 3D radial acquisition results in prolonged reconstruction time, therefore, the feasibility of CS for high resolution 3D radial acquisition for accelerating 3D CMR has not been previously demonstrated.

Recently, graphics processing units (GPU) have become available for highly computationally intensive applications, and using GPU for general purpose computation has gathered great interests in many research areas that require heavy computational overload. The hardware manufacturers are providing parallel computing architectures (such as CUDA and FireStream) that enable researchers to implement GPU programs using high level programming languages without knowledge of the GPU hardware structure. Recent studies have shown that GPU-accelerated reconstruction can be used to achieve reduced and low-latency reconstruction time for various MR applications: The gridding algorithm for 2D radial and spiral trajectories [70], the non-Cartesian SENSE and non-Cartesian k-t SENSE reconstruction [71], total variation regularized reconstruction for undersampled stack-of stars trajectories in MR angiography [72], and so on. It has been shown that GPU implementations can provide order of magnitude reduction in the reconstruction time, for example, GPU-accelerated reconstruction for 2D radial acquisition demonstrated with approximately 6-32 times speed-up in reconstruction time compared to CPU implementations [70, 73]. GPU implementations have been shown to greatly accelerate CS reconstructions of 3D non-Cartesian trajectories such as stack-of-radials and stack-of-spirals [72, 74]. The stack-of-radials/spirals trajectories, however, are sampled equi-distant along one k-space dimension, allowing the reconstruction of the MR image to be the same as multiple 2D non-Cartesian reconstructions with an additional one dimensional inverse Fourier transform on the equidistantly-sampled direction. While the benefits of GPU implementation on the reconstruction of 2D non-Cartesian trajectories have been previously demonstrated, GPU implementation for a true 3D non-Cartesian trajectory such as 3D radial sampling is not as straightforward and has not been previously reported due to the large size of the 3D sampling data and GPU hardware limitations.

In this chapter, the iterative CS reconstruction for highly undersampled 3D radial trajectory was implemented using commodity GPU hardware.

3.1 Materials and Methods

3.1.1 GPU Programming Structure

The CS reconstruction for 3D radial trajectory was implemented using Compute Unified Device Architecture (CUDA, Nvidia, Santa Clara, CA) environment, which provides a simple extension of the standard C language for GPU programming. Generally CUDA programs consist of two parts: host program that is executed on CPU, and device program that is executed on GPU. The code which has little or no parallelism in computation is written in host code using ANSI C language, and the code which has a large amount of parallelism in computation is written in device code using a slightly modified C-like language. The functions written in the device code are called *kernels*, and each kernel generates a large number of *threads* as a result of data parallelism once the kernel is invoked. All the threads generated by a kernel invocation are called a *grid*. The threads in a grid are grouped into *blocks*, which are the basic allocation unit for the execution resources on the hardware. All the blocks in the same grid must have the same number of threads. Blocks can have 1D or 2D structure, and the threads can have 1D, 2D or 3D structure.

3.1.2 Implementation of CS Reconstruction for 3D Radial Trajectory

The iterative CS reconstruction for 3D radial trajectory in Chapter 2 involves FFT/IFFT , the gridding/re-gridding operations and the sparsifying transform and its inverse operation at every iteration. The gridding and re-gridding operations are the most computationally intensive part of the iterative CS reconstruction. Since the width of the convolution window is much smaller than the size of the entire k-space, the gridding/re-gridding operations for each measured radial point are highly localized and can be performed in a parallel manner for each measured radial point, and are well-suited for CUDA implementation. In this chapter, we assigned each 3D radial data point to one CUDA thread. Each projection line corresponds to one block, which consists of N_s threads. The grid has 2D block structure (N_p, N_i) to represent all the projection lines and interleaves of the 3D radial trajectory. Figure 3.1 shows a simplified example of a grid hierarchy and thread assignment of our implementation, where we have 8 sample points in one projection, 3 projection lines per interleaf, and 2 interleaves. In the gridding operation, contributions from adjacent radial samples are accumulated to a Cartesian sample point as illustrated in Figure 3.2(a), which results in accumulative memory writes during the parallelized execution. The accumulative memory writes can produce incorrect results if more than two threads try to access the same memory simultaneously. This was prevented by using CUDA's atomic operation, which is capable of reading and writing on a memory address without interruption by other threads, allowing concurrent threads to correctly perform the required memory access. The performance of atomic operation in CUDA is greatly improved on recent "Fermi"-based GPUs offered by Nvidia, which provide up to 20 times faster atomic operation compared to the their former generation GPUs [75].

Besides the gridding/re-gridding operations, most of the CS reconstruction procedures including FFT/IFFT, wavelet/inverse-wavelet transforms, de-apodization and thresholding were parallelized and written in device code. cuFFT and cuBLAS packages were used for FFT/IFFT and other arithmetic operations. Due to the limited global memory size of current GPU hardware, we could not parallelize the reconstruction for the multiple coil elements. The reconstruction was performed sequentially for each coil and the final reconstructed image was obtained as the root-sum-square of the individual coil images. The CS reconstruction was also implemented in standard C++ environment for the comparison of the reconstruction time. The FFTw package (41) was used for FFT/IFFT operations. The GPU and C++ implementations of the CS reconstruction were based on single precision floating point arithmetic, and they were executed on a PC with Intel (Santa Clara, CA) Core2 Quad Q9400 CPU (2.66 GHz) , 8.0 GB memory, and NVIDIA GeForce GTX 480 Graphics card (480 cores, 1.5 GB memory) running on a 64 bit Windows 7 operating system.

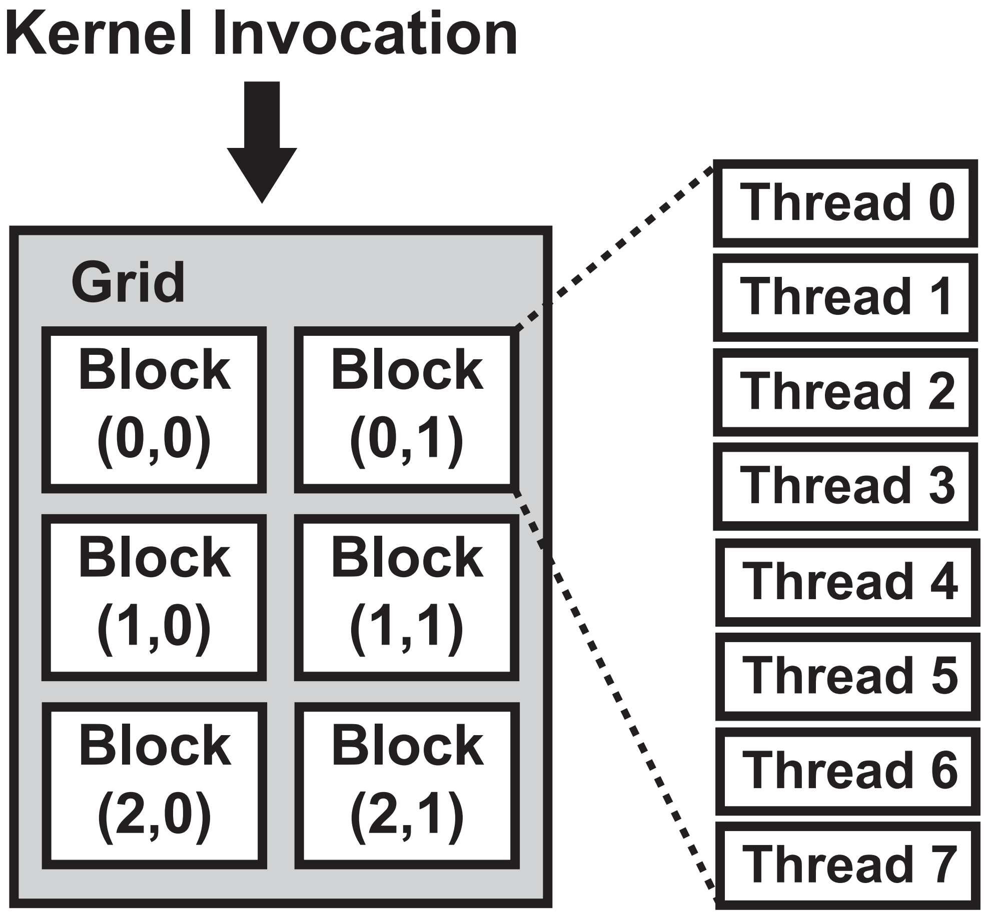

Figure 3.1: CUDA grid hierarchy and thread assignment: A grid, which consists of multiple threads, is generated once the device kernel is invoked. Each projection line of the 3D radial trajectory is assigned to one block of threads. Each thread in a block corresponds to a 3D radial sample point in the same projection line. The total number of projections is equal to the total number of blocks. This example shows a thread assignment of a 3D radial trajectory with $(N_s, N_p, N_i) = (8, 3, 2)$.

3.1.3 Experiments

The CS reconstruction was performed on four different whole heart MRI data sets. The number of samples per projection and the number of interleaves were kept fixed as $N_s = 392$ and $N_i = 10$, and the data were acquited with four different sampling densities $(10\%, 20\%, 30\%$ and $40\%)$, which determined the number of projections per interleaf to be $N_p = 396, 768, 1152$ and 1536, respectively.

The CS reconstruction was also implemented using standard C++ environment, and the reconstruction was performed on the same MRI data sets. The execution time for the completion of one iteration of the CS reconstruction with CUDA and C++ implementations were measured and compared. The execution time for each component operation, i.e., gridding/re-gridding, FFT/IFFT and thresholding were also measured and compared. The measurement of the execution time was averaged over 100 iterations.

3.2 Results

The execution time of the iterative CS reconstruction for 3D radial trajectory was compared between the CUDA and the C++ implementations. Table 3.1 shows the average time required for the completion of one iteration of the iterative CS reconstruction with CUDA and C++ implementations. The reconstruction was performed on the in-vivo data for 4 different sampling densities (10%, 20%, 30% and 40%), which correspond to the sampling parameters $(N_s, N_p, N_i) = (392, 396, 10)$, $(392, 768, 10)$, $(392, 1152, 10)$, and $(392, 1536, 10)$, respectively. The measured time is averaged over

100 iterations. The speed up of the CUDA implementation over the C++ implementation was reported to be 56.5 $\sim$ 58.8 for the gridding operation and 111.5 $\sim$ 111.8 for the re-gridding operation. The execution time of gridding operation was almost twice longer than the execution time of re-gridding operation in CUDA implementation for a given sampling density, while the execution time of gridding and re-gridding operations were nearly the same for C++ implementation. The gridding operation in CUDA is hampered by the heavy accumulative memory writes which the re-gridding operation is free of, and this results in the increased execution time even if gridding and re-gridding operations have the same thread configuration. It is mentioned in Section 3.1.2 that the atomic operation of Fermi-based GPU has been greatly improved, but it is still less efficient than the operations without cumulative memory access for parallel implementation. The execution time of FFT/IFFT was kept almost constant over different sampling densities for both CUDA and C++ implementations, as the size of reconstruction matrix was the same for all data sets ($392 \times 392 \times 392$) Overall, the speed up of the CUDA implementation was 34.3, 43.7, 50.2 and 53.9 for 10%, 20%, 30% and 40% sampling densities, respectively. The total execution of the CS reconstruction for 20% sampled data takes 85.74 seconds in C++ implementation and 1.96 seconds in CUDA implementation, yielding 43.7 times speedup. With a 5 channel phased-array coil and 1000 iterations, the reconstruction of a 3D radial acquisition will take around 5 days in C++ implementation, while it takes around two and a half hours in CUDA implementation. The images reconstructed by CUDA implementation were visually identical to those reconstructed by C++ implementation for all the 3D radial data sets we have tested.

(N_s, N_p, N_i)	$(392, 396, 10)$			$(392, 768, 10)$			$(392, 1152, 10)$			$(392, 1536, 10)$		
	CUDA	C++	SU	CUDA	C++	SU	CUDA	C++	SU	CUDA	C++	SU
FFT	0.27s	5.00s	18.5	0.26s	5.01s	18.7	0.27s	4.99s	18.5	0.27s	4.99s	18.2
IFFT	0.27s	5.04s	18.6	0.26s	5.06s	18.8	0.27s	5.04s	18.7	0.27s	5.06s	18.6
Gridding	0.31s	17.59s	56.5	0.58s	34.04s	58.1	0.86s	51.00s	58.7	1.15s	67.84s	58.8
Re-gridding	0.15s	17.64s	111.5	0.30s	34.12s	111.8	0.45s	51.11s	111.8	0.60s	67.99s	111.6
Thresholding	0.01s	1.10s	69.1	0.01s	1.10s	68.6	0.01s	1.10s	68.7	0.01s	1.09s	67.1
Etc.	0.50s	6.07s	-	0.51s	6.39s	-	0.50s	6.41s	-	0.52s	6.45s	-
Total (CS-image)	**1.52s**	**52.48s**	**34.3**	**1.96s**	**85.74s**	**43.7**	**2.38s**	**119.68s**	**50.2**	**2.84s**	**153.44s**	**53.9**
DWT	0.24s	8.51s	35.5	0.24s	8.51s	35.5	0.24s	8.53s	35.5	0.24s	8.51s	35.5
IDWT	0.21s	8.72s	41.5	0.21s	8.74s	41.6	0.21s	8.74s	41.6	0.21s	8.74s	41.6
Total (CS-wavelet)	**1.97s**	**69.71s**	**35.4**	**2.41s**	**102.99s**	**42.7**	**2.83s**	**136.95s**	**48.4**	**3.29s**	**170.69s**	**51.9**

Table 3.1: Average time required for performing main operations in one iteration of the CS reconstruction for each coil with CUDA and C++ implementations for a 3D radial data of size (N_s = # samples, N_p = # projections, N_i = # interleaves) and associated speed up (SU).

3.3 Discussion

For CUDA implementation of the gridding/re-gridding operations in the iterative CS reconstruction, the computations can be assigned to the device code either by dividing the 3D radial data points among threads (*radial point driven*) or by dividing the Cartesian grid points among threads (*Cartesian point driven*). The radial point driven assignment is a simple and intuitive approach and has minimum number of memory reads (writes) in gridding (re-gridding), but results in a large amount of data sharing among threads and accumulative memory writes in gridding as illustrated in Figure 3.2(a). Each CUDA thread assigned to the radial data point will read the memory to get the measured k-space value for the sample point and distribute the value to the neighboring Cartesian grid points inside the convolution window. The Cartesian grid point will have different contributions from different radial sample points, resulting in cumulative memory access among different CUDA threads. In our experiment, the execution time of the gridding operation was only twice as long as the re-gridding operation despite the massive cumulative memory access and atomic operations. On the other hand, the Cartesian point driven assignment has minimum number of memory writes (reads) in gridding (re-gridding). However, one must compute the list of the radial points associated with the Cartesian grid point within the convolution window for every thread, which requires additional computations and/or additional memory usage. The Cartesian point driven assignment is illustrated in Figure 3.2(b). Each CUDA thread assigned to the Cartesian grid point will read the memory to get the measured k-space values from neighboring radial sample points inside the convolution window, combine the values and write on the memory for the

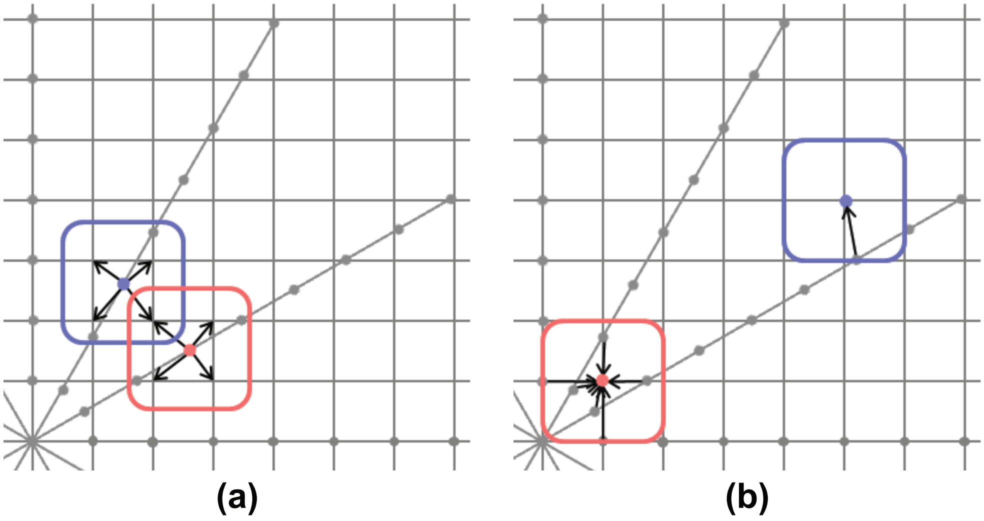

Figure 3.2: Thread assignment strategies for implementation of a gridding algorithm in CUDA programming: (a) radial point driven assignment, (b) Cartesian point driven assignment. Cumulative memory writes can be observed in the radial point driven assignment. The central grid point has a larger workload than the outer grid point in the Cartesian point driven assignment.

Cartesian point only once. The Cartesian point driven assignment has an uneven workload distribution over different threads, and it causes poor *compute to global memory access ratio* for outer k-space points, especially at low sampling densities. Each thread assignment strategy has its advantage and disadvantage, and it is not simple to determine which one is superior to the other. In this study, we used radial point driven assignment; more study and optimization on the thread allocation and memory management can be done as a future work for further speed-up of the parallel implementation.

The proposed implementation of the 3D radial acquisition still takes a long time to be clinically feasible. For example, we have used 3000 iterations for the CS reconstruction of the phantom data (344^3 voxels) and 1000 iterations for the in-vivo data (392^3 voxels), and the final reconstruction times for the data with 20% sampling density were around 5 hours and 2.5 hours, while the conventional gridding algorithm takes a few minutes with the C++ implementation for any case. However, CS reconstruction with fewer iterations (e.g. 100 iterations) still provides improved image quality compared to the gridding algorithm, and the reconstruction time in this case is around 10-16 minutes with 20% sampling density with the GPU implementation.

3.4 Conclusion

We have implemented a GPU-accelerated iterative CS reconstruction method for highly undersampled 3D radial trajectory and compared its performance with C++ implementation. The GPU implementation reduced the reconstruction time substantially, enabling the feasibility of CS reconstruction for 3D radial acquisition.

Chapter 4

Compressed Sensing Reconstruction for Undersampled Breath-Hold Radial Cine Imaging with Auxiliary Free-Breathing Data

Segmented cine magnetic resonance (MR) imaging (MRI) allows non-invasive and reproducible evaluation of the cardiac function. Clinically, cine imaging is acquired in a multi-slice breath-hold acquisition where one or two slices are acquired within a breath-hold (BH) and the patient will breathe normally for a period of 20-30 second between BHs. As the spatiotemporal resolution of the cine imaging increases, the number of heartbeats required for the segmented acquisition and the duration of the

BH increase. To improve the imaging throughput, multiple slices are acquired within a BH to reduce total scan time spent for evaluation of cardiac function. In patients with difficulty in breath-holding or pediatric patients, real-time cine or segmented cine in short BH is used. For multiple-BH acquisitions to cover the entire left ventricle (LV), majority of time is devoted to resting period between scans so as the patient recover from BH. In a typical patient for a 10 second BH, 20-30 second is spent in between BHs, which results in substantially low acquisition efficiency of 30-50%.

Acceleration techniques for dynamic or cine MRI have been widely studied. Unaliasing by Fourier-encoding the overlaps using the temporal dimension (UNFOLD) utilizes temporal filtering to remove the aliasing undersampling artifacts [76], temporal sensitivity encoding (TSENSE) exploits coil sensitivity information and temporal filtering [77], and k-t Broad-use Linear Acquisition Speed-up Technique (k-t BLAST) utilizes object-specific information obtained from the training data [78]. More recently, compressed sensing (CS) technique [64] has been applied for various MRI reconstruction problems by using the compressibility of MR images in appropriate transform domains. Feasibility of the use of CS for reconstruction of dynamic images exploiting spatial domain and temporal frequency domain as the sparsifying transform domain (x-f space sparsity) was also presented [79]. Although Cartesian trajectories are often used for cardiac cine imaging, non-Cartesian trajectory such as radial trajectory [80] can also be used. Radial trajectory has different imaging properties that may be favorable to the cine imaging: Radial trajectory has inherent advantages for object motion [81, 82, 83], radial undersampling does not yield a substantial decrease in spatial resolution as the spatial resolution is mainly determined by the k-space coverage [84], and the streaking artifacts in an undersampled radial acquisition are more tolerable compared to the ghosting artifacts in an undersampled Cartesian acquisition [32]. Acceleration techniques for radial trajectories have also been proposed. Radial focal undetermined system solver (FOCUSS) [85] asymptotically provides l_1 minimized CS reconstruction, GRAPPA [43] operator is used in conjunction with GROG [45] to reconstruct undersampled non-Cartesian data sets in [86], and total variation constraint is used for undersampled radial data with multiple coils in [41]. k-t BLAST and k-t FOCUSS have been extended to radial trajectories in [87] and [88], respectively.

In this chapter, we propose to take advantage of the resting periods between BHs to acquire additional auxiliary free-breathing (FB) data that can be used in the reconstruction of undersampled radial BH acquisition in order to improve the image quality without increasing the total scan time. Cardiac function measurements calculated from accelerated radial cine images, reconstructed using conventional gridding [40], CS with x-f space sparsity and the proposed accelerated cine reconstruction using additional auxiliary FB scan are compared to evaluate the feasibility of the proposed approach.

4.1 Materials and Methods

4.1.1 Radial Cine Acquisition and the CS Reconstruction

The acquisition and the CS reconstruction of the radial cine imaging are illustrated in Figure 4.1(a). An undersampled BH acquisition is followed by a fully-sampled FB acquisition during the resting period between BH acquisitions. The undersampled radial cine data is reconstructed using CS by minimizing the following objective function:

$$J(\mathbf{x}_i) = ||\mathbf{A}\mathbf{x}_i - \mathbf{y}_i||_2^2 + \lambda\Psi(\mathbf{x}_i), \tag{4.1}$$

where $\mathbf{x}_i$ denotes the i-th cardiac phase image, $\mathbf{y}_i$ denotes the undersampled radial k-space measurement for i-th cardiac phase, A is the encoding matrix of the radial acquisition, and Ψ is a transform operator that sparsifies the image in the transform domain, and λ is a positive scalar parameter that determines the tradeoff between the consistency of the measured k-space data and the sparsity level of the reconstructed image. In our study, the difference image from the additionally-acquired fully-sampled FB data is used as the sparsifying operator as $\Psi(\mathbf{x}_i) = ||\mathbf{x}_i - \mathbf{x}_{FB,i}||_1$, where $\mathbf{x}_{FB,i}$ is the i-th cardiac phase image from the fully-sampled FB acquisition. Each cardiac phase image is sparsified by subtracting the image reconstructed from the fully-sampled FB acquisition with the same cardiac phase for successful CS reconstruction. The fully-sampled FB images are reconstructed by the conventional gridding algorithm [40]. The FB images are fully-sampled and thus do not have the streaking artifacts coming from the undersampling of the radial trajectory. The FB images are, however, acquired while the patient is breathing normally, and the respiratory motion is averaged over multiple cardiac cycles resulting in blurry images. Figure 4.2 illustrates example cardiac phases from fully-sampled BH and FB acquisition and the difference images. The FB acquisition yields blurry images due to the respiratory motion compared to the BH acquisition, and the sparseness of the difference images can be appreciated. The difference images contain non-zero elements only in the areas where there are cardiac and/or respiratory motion, because the static regions from the BH and FB images have similar signals and cancelled out each other. To minimize the objective function in Equation 4.1, we adopt an iterative method which alternately enforces the data consistency and the sparsity of the image estimate at every iteration as in Chapter 2. The intermediate image update at the $(t+1)$-th iteration is obtained by solving the following two sub-problems:

$$\mathbf{u}_i(t) = \mathbf{x}_i(t) + \frac{1}{\alpha_t}\mathbf{A}^* \left(\mathbf{y}_i - \mathbf{A}\mathbf{x}_i(t)\right), \tag{4.2}$$

which is called the data consistency step and

$$\mathbf{x}_i(t+1) = \arg\min_{\mathbf{x}} \frac{1}{2}||\mathbf{x} - \mathbf{u}_i(t)||_2^2 + \frac{\lambda}{\alpha_t}\mathbf{\Psi}(\mathbf{x}), \tag{4.3}$$

which is called the thresholding step. Equation (4.3) can be efficiently solved by a coefficient-wise thresholding function for the case of the difference operator $\mathbf{\Psi}(\mathbf{x}_i) = ||\mathbf{x}_i - \mathbf{x}_{FB,i}||_1$ as

$$x_i^n(t+1) = x_{FB,i}^n + \frac{u_i^n(t) - x_{FB,i}^n}{|u_i^n(t) - x_{FB,i}^n|} \max\left(|u_i^n(t) - x_{FB,i}^n| - \frac{\lambda}{\alpha_t}, 0\right), \tag{4.4}$$

where the superscript n denotes the n-th element of the input image vector. for the step size parameter α_t, we adopt the update rule from [55].

4.1.2 Undersampling Pattern

For the undersampled BH acquisition, the radial trajectory is uniformly undersampled to have a constant angle between adjacent projection lines, since it has been shown that uniform undersampling provides superior image quality compared to random undersampling with CS reconstruction [89]. The sampling pattern is varied for

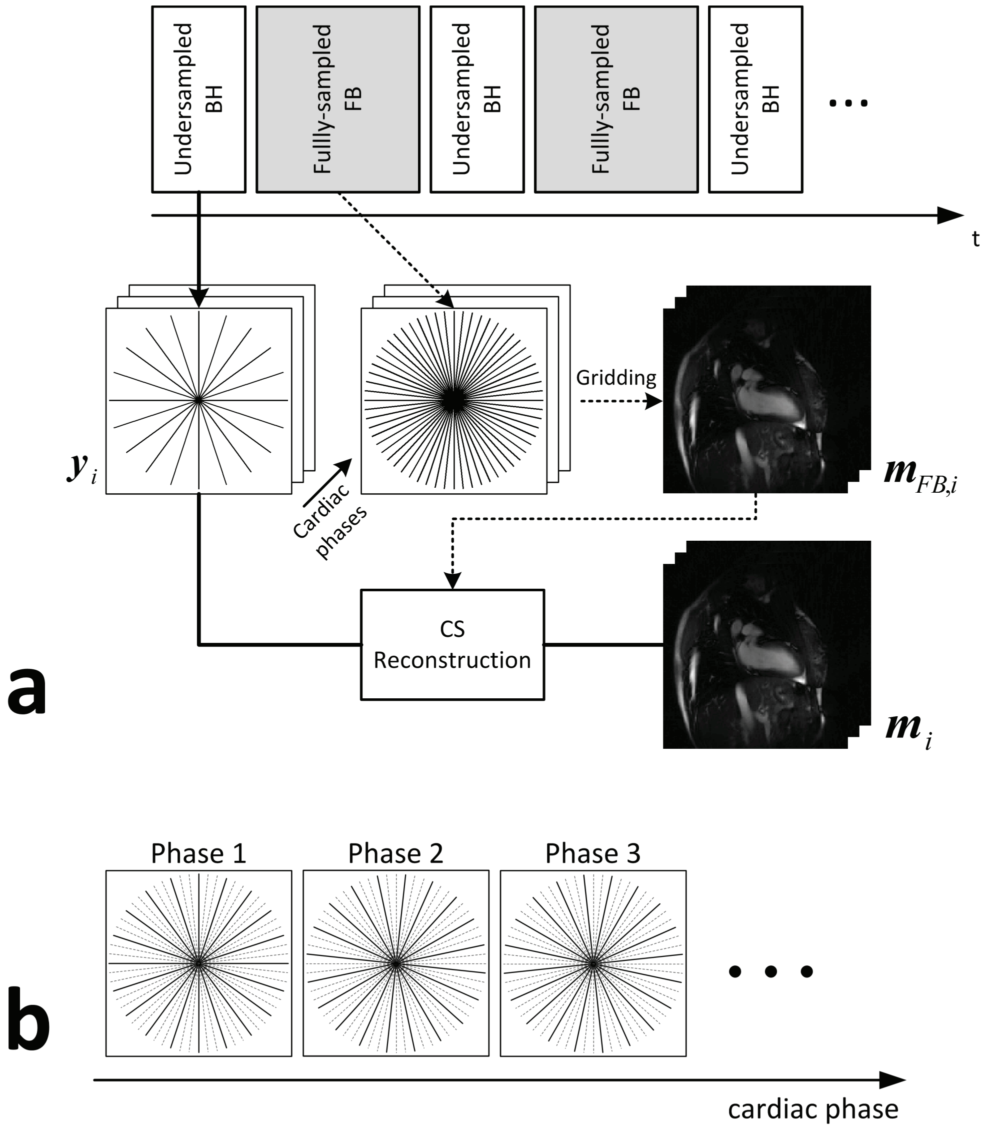

Figure 4.1: a) Illustration of the proposed radial cine acquisition.. The undersampled BH acquisition is followed by a fully-sampled FB acquisition between BH acquisitions. The fully-sampled FB data is reconstructed by the conventional gridding algorithm and then used for the CS reconstruction of the undersampled BH data for each cardiac phase. b) Undersampling pattern for different cardiac phases of the BH acquisition. The sampling pattern is rotated by one sampling angle per cardiac phase.

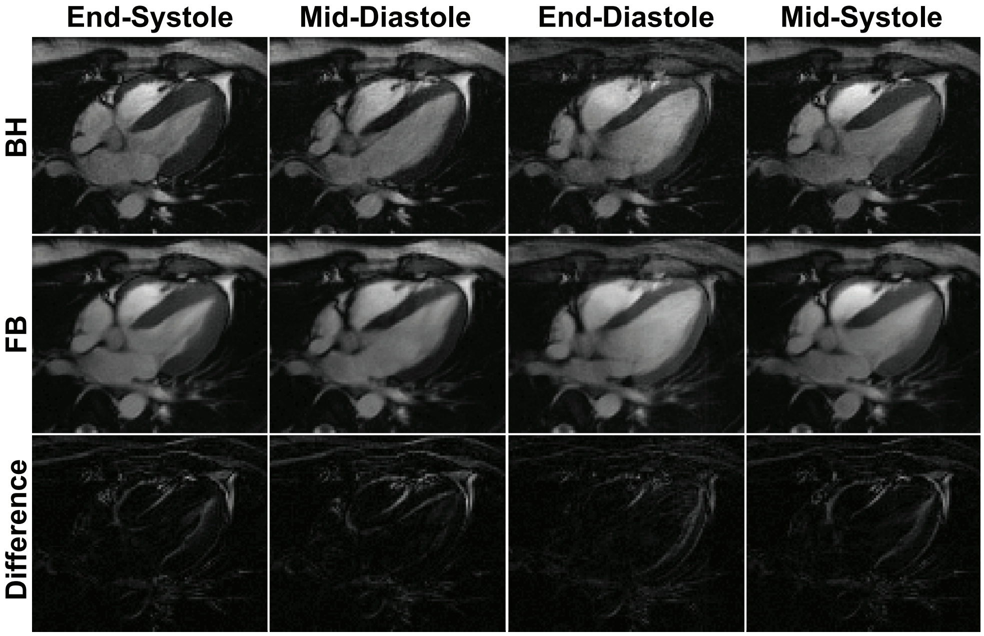

Figure 4.2: Exemplary cardiac phase images from fully-sampled BH acquisition, fully-sampled FB acquisition, and the difference images. The images from FB acquisition are blurred due to the respiratory motion. The difference images are sparse and contain non-zero elements only in the areas where there are respiratory/cardiac motion.

different cardiac phases and it is rotated by $\frac{180°}{N_{Full}}$ per cardiac phase where N_{Full} is the number of projection lines in the fully-sampled radial trajectory as illustrated in Figure 4.1(b). This time-varying undersampling is not required for the proposed CS reconstruction as the proposed method reconstructs each cardiac phase image independently and does not utilize any temporal dependency between different cardiac phases. This sampling pattern is used in order to introduce incoherent aliasing artifacts in the temporal frequency domain for the reconstruction of the conventional CS based on x-f space sparsity.

4.1.3 In Vivo Study

Ten healthy subjects were imaged with an ECG-triggered steady-state free precession (SSFP) sequence. The scan parameters were as follows: number of cardiac phases = 20, field-of-view (FOV) = (320 mm)^2, spatial resolution = (1.7 mm)^2, TR/TE/α = 3.1/1.5/55. All BH and FB acquisitions were acquired fully-sampled, and the BH acquisition was retrospectively undersampled to the undersampling rate of R = 3 and 5, which yield 33% and 20% sampled data sets. Total of four fully-sampled data sets were acquired for each imaging plane: the first data set was acquired during BH and the remaining three data sets were acquired during FB. The three FB data sets were averaged and then used for the reconstruction of $\mathbf{x}_{FB,i}$. The fully sampled dataset acquired during BH, were undersampled retrospectively to evaluate the reconstruction algorithm. The reference images were obtained from the fully-sampled BH data sets by using the conventional gridding reconstruction algorithm, and the undersampled BH data sets were reconstructed by the gridding algorithm, the conventional CS reconstruction using x-f space sparsity and the proposed CS reconstruction with the auxiliary FB data sets.

4.1.4 Data Analysis

For the quantitative assessment of the study, the sharpness of the blood-myocardium border was measured and compared on the images reconstructed by the gridding algorithm with fully sampled reference BH data, the conventional CS reconstruction using x-f space sparsity with the undersampled BH data, and the proposed CS reconstruction with the undersampled BH data. The sharpness was measured from the signal intensity profile of a straight line perpendicularly crossing the blood-myocardium border. The sharpness score was defined as the reciprocal of the distance (mm) between the two points which have 20% and 80% of the signal intensity of the profile [90].

The performance of the proposed CS reconstruction was further evaluated by measuring the cardiac volumes and the ejection fraction of the left ventricle (LV). The reconstructed cine images were written into DICOM format and transferred to the ViewForum workstation (Philips Healthcare, Best, the Netherlands) for the analysis. The LV end-diastolic volume (LVEDV), LV end-systolic volume (LVESV) and LV ejection fraction (LVEF) were measured by a board certified cardiologist with level 3 training in cardiac MRI blinded to the method of reconstruction using a commercially available software included in the ViewForum workstation.

4.2 Results

Figures 4.3, 4.4 and 4.5 show exemplary cardiac phase images in 2-chamber (2CH), horizontal long axis (HLA) and short axis (SAX) views reconstructed by conventional CS algorithm with x-f space sparsity and the proposed CS algorithm. The reference images reconstructed by the gridding algorithm from fully-sampled data set were also included for comparison. The BH data are undersampled to have 33% and 20% of projections from fully-sampled data. While both CS reconstructions remove most of the streaking artifacts efficiently, the proposed CS reconstruction exhibits sharper blood-myocardium borders and improved image quality.

The blood-myocardium border sharpness scores are measured on the images reconstructed by the gridding reconstruction with the fully-sampled BH data, the conven-

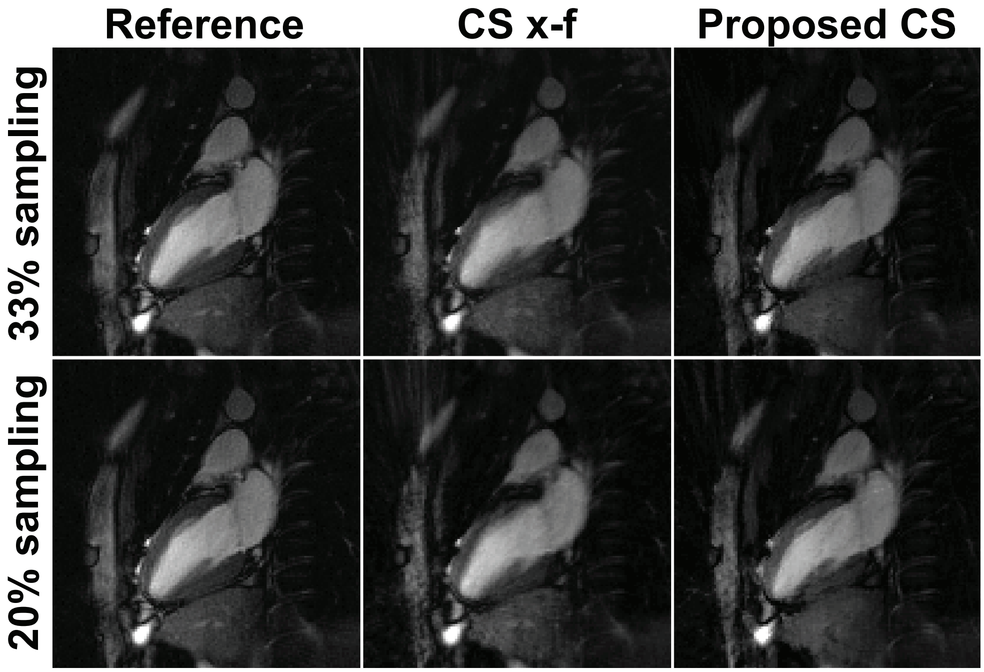

Figure 4.3: Example cardiac phase images in 2-chamber (2CH) views from 33% sampled and 20% sampled data sets reconstructed by the conventional CS reconstruction with x-f space sparsity (CS x-f), and the proposed CS reconstruction with additional FB data. The reference images were reconstructed by the conventional gridding algorithm from fully-sampled data set. The proposed CS reconstructions exhibit less streaking artifacts, improved sharpness and improved image quality compared with the conventional CS reconstruction.

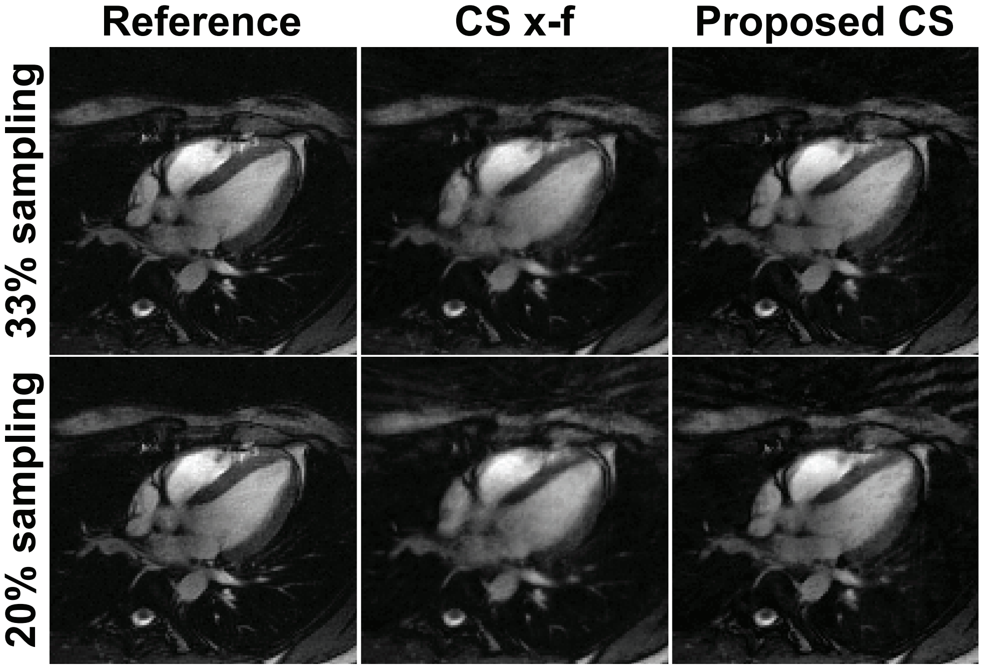

Figure 4.4: Example cardiac phase images in horizontal long axis (HLA) views from 33% sampled and 20% sampled data sets reconstructed by the conventional CS reconstruction with x-f space sparsity (CS x-f), and the proposed CS reconstruction with additional FB data. The reference images were reconstructed by the conventional gridding algorithm from fully-sampled data set. The proposed CS reconstructions exhibit less streaking artifacts, improved sharpness and improved image quality compared with the conventional CS reconstruction.

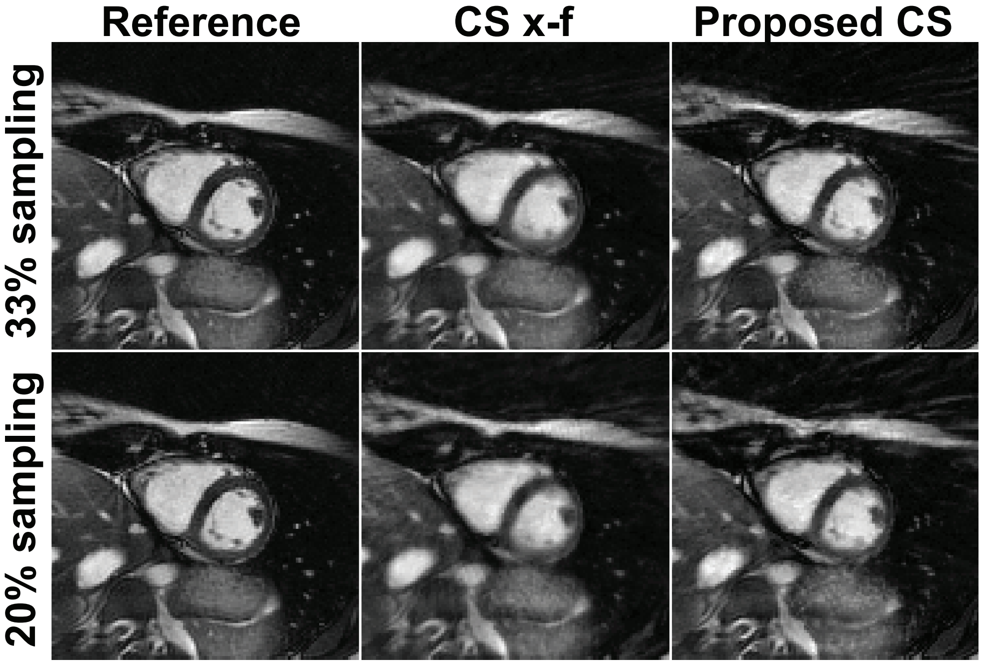

Figure 4.5: Example cardiac phase images in short axis (SAX) views from 33% sampled and 20% sampled data sets reconstructed by the conventional CS reconstruction with x-f space sparsity (CS x-f), and the proposed CS reconstruction with additional FB data. The reference images were reconstructed by the conventional gridding algorithm from fully-sampled data set. The proposed CS reconstructions exhibit less streaking artifacts, improved sharpness and improved image quality compared with the conventional CS reconstruction.

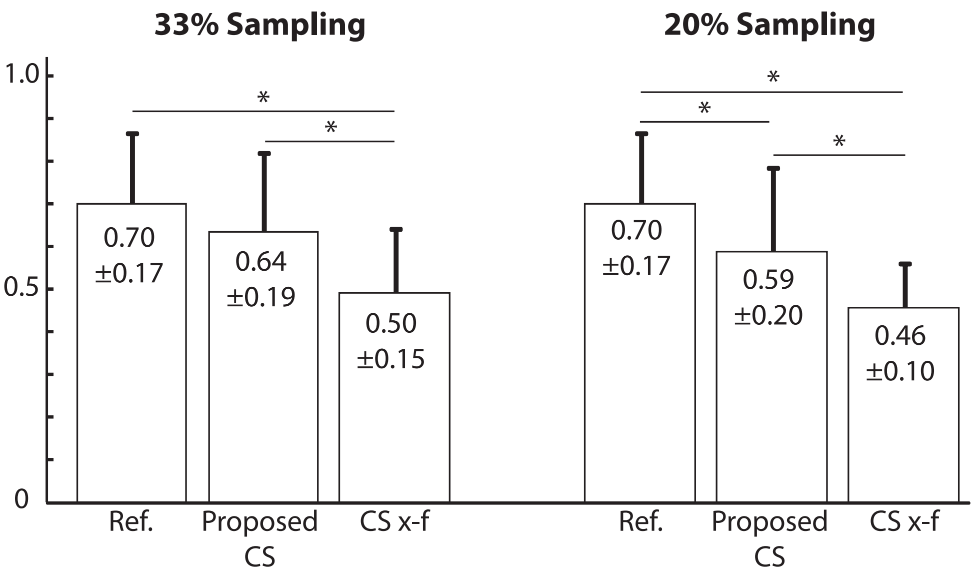

Figure 4.6: The blood-myocardium border sharpness scores of the reference images from the fully-sampled BH data, the proposed CS reconstructions, and the conventional CS reconstructions (CS x-f) with 33% and 20% sampled data sets. (*: $P < 0.05$)

tional CS reconstruction using x-f space sparsity with the undersampled BH data and the proposed CS reconstruction with the undersampled BH data and the additional FB data. The measured blood-myocardium border sharpness scores are summarized in Figure 4.6. The sharpness scores for the reference images from the fully-sampled BH data and the proposed CS reconstructions were both significantly higher than the conventional CS reconstructions using x-f space sparsity with 33% sampled data set. The sharpness score for the proposed CS reconstruction with 33% sampled data set was similar to that of the reference image. The sharpness score for the proposed CS reconstruction with 20% sampled data set was lower than that of the reference image but it was significantly higher than that of the conventional CS reconstruction with 20% sampled data set.

The LVEDV, LVESV and LVEF were measured from the SAX images reconstructed by the four reconstruction methods (gridding reconstruction with fully-sampled data, gridding reconstruction with undersampled data, conventional CS reconstruction using x-f space sparsity with undersampled data, and proposed CS reconstruction with the undersampled data), and the results are summarized in Table 4.1. The proposed CS reconstruction and the gridding reconstruction of 33% sampled data provide LVEDV, LVESV and LVEF values similar to the fully-sampled images with the confidence interval of 95%, while the conventional CS reconstruction using x-f sparsity provides under-estimated LVEDV and LVEF values. For 20% sampled data, only the proposed CS reconstruction provides similar LVEF value to the fully-sampled reference. It is noted that the LVEDV and LVESV values of the gridding reconstruction with 20% sampled data were not significantly different from those of the fully-sampled reference, but the LVEF value was different from that of the reference. The Bland-Altman plots of the LVEDV, LVESV and LVEF for the proposed CS reconstructed images vs. the fully-sampled reference images are given in Figure 4.7 and 4.8. The Bland-Altman analysis indicates that the agreement between the fully-sampled reference images and the proposed CS reconstructed images with 95% confidence interval were -0.6±5.8 mL for LVEDV, 1.7±5.3 mL for LVESV and -1.4±2.9% for LVEF with 33% sampled data sets, and -4±5.1 mL for LVEDV, -2.2±2.9 mL for LVESV and 0.4±1.9% for LVEF with 20% sampled data sets. Linear regression is performed on the LV measurements for the proposed CS reconstruction vs. fully-sampled reference, and the slopes of the regression are reported as 0.9224, 1.029, and 0.9800 for LVEDV, LVESV and LVEF with 33% sampled data, and 0.9477, 0.9587, and 0.9892 for LVEDV, LVESV and LVEF with 20% sampled data, respec-

	Reference	Gridding		CS x-f		Proposed CS	
Density	100%	33%	20%	33%	20%	33%	20%
LVEDV	142.2±21.2	140.7±17.3	133.9±21.3	132.6±21.5$^{*,\#}$	123.8±22.1$^{*,\#}$	141.6±18.0	134.6±22.0*
LVESV	56.8±16.7	57.5±16.4	59.0±17.8	58.6±17.5	57.8±17.2$^{\#}$	58.5±17.8	54.6±15.7*
LVEF	0.61±0.08	0.60±0.09	0.57±0.11*	0.57±0.09$^{*,\#}$	0.54±0.09$^{*,\#}$	0.59±0.10	0.60±0.07

Table 4.1: Comparison of the measured LVEDV, LVESV (mL) and LVEF (%) from SAX images reconstructed by the gridding reconstruction, conventional CS reconstruction with x-f space sparsity (CS x-f) and the proposed CS reconstruction for 33% and 20% undersampled data sets. (*: $P < 0.05$ from the reference, #: $P < 0.05$ from the proposed CS)

tively. The corresponding R^2 values were 0.8984, 0.9106 and 0.9051 with 33% sampled data and 0.9393, 0.9708 and 0.9225 with 20% sampled data, respectively.

4.3 Discussion

In this chapter, we have proposed an accelerated radial cine acquisition strategy and a CS reconstruction algorithm, where the additional FB acquisition acquired during the resting period is utilized to improve the CS reconstruction of the BH acquisition. We have evaluated the performance of the proposed CS reconstruction and compared with the conventional CS reconstruction using x-f space sparsity and conventional gridding. The reconstructed images show that the proposed CS reconstruction yields sharper blood-myocardium border scores and provides better image quality for the assessment of LV volumes and LVEF than the conventional CS reconstruction.

Many CS reconstruction methods have been proposed to improve the reconstruction of undersampled MRI data in various applications. Most of the CS reconstruc-

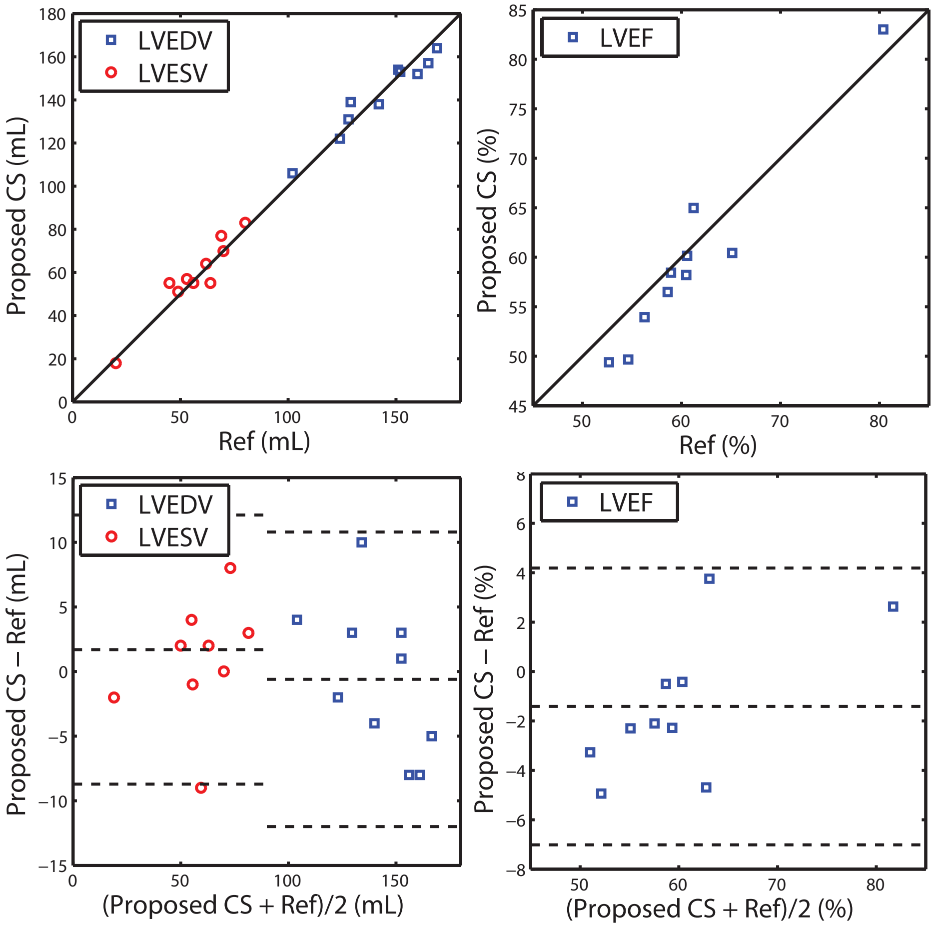

Figure 4.7: Comparison of LVEDV, LVESV and LVEF measurements of the fully-sampled reference images and the proposed CS reconstructed images based on correlation and Bland-Altman plots. The proposed CS reconstruction is performed on 33% sampled data sets.

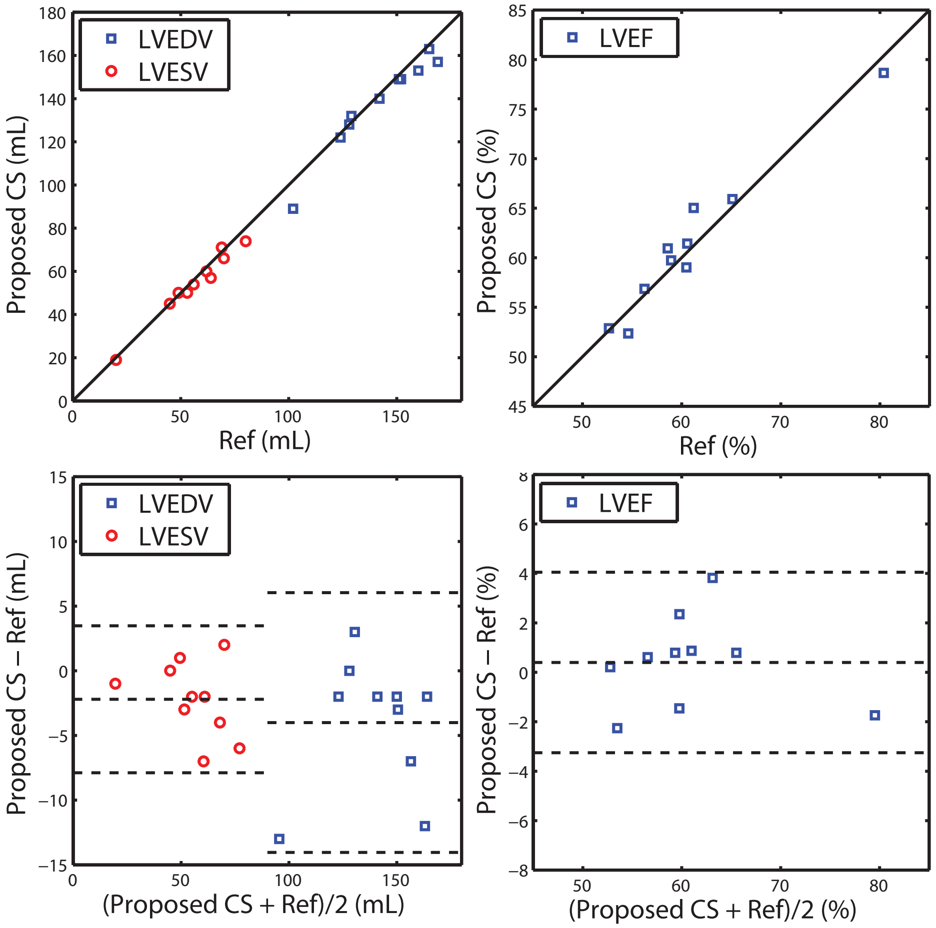

Figure 4.8: Comparison of LVEDV, LVESV and LVEF measurements of the fully-sampled reference images and the proposed CS reconstructed images based on correlation and Bland-Altman plots. The proposed CS reconstruction is performed on 20% sampled data sets.

tion methods utilize a predetermined sparsifying transform such as wavelet, finite differences and x-f space. It is not possible, however, to predict whether a given transform can efficiently represent the underlying image characteristic and provide a sufficiently sparse image. For instance, wavelets cannot capture smooth transitions sparsely, whereas finite differences have problem with sharp edges. More sophisticated techniques have been proposed that can adaptively capture objective-specific sparsity nature [68, 69]. The proposed method in this paper utilizes the fully-sampled FB acquisition of the same cardiac phase for the reconstruction of the undersampled BH acquisition, therefore can provide object-specific sparse representation in a simple way to improve the CS reconstruction, based on the basic assumption of segmented cine acquisition that the cardiac motion is consistent over different cardiac cycles.

The proposed CS reconstruction has provided sharper images, while the conventional CS reconstruction with x-f space sparsity has provided slightly blurry images. The blurring of the reconstructed images in the conventional CS was not reported in the original study [91] for an undersampling factor of three (33% sampling). The results cannot be directly compared because the original paper uses Cartesian trajectories. While it is not difficult to design a random undersampling pattern in k_y-t domain for successful CS reconstruction in Cartesian trajectory since k_x direction (readout direction) is always fully-sampled, it is not straightforward to design an undersampling pattern in radial trajectory because the readout direction is changing and all three directions (k_x, k_y and t) need to be considered at the same time. The undersampling pattern of k_x-k_y-t domain for x-f space sparsity has not been studied for radial trajectories. We have used a rotating sampling pattern by one projection angle per cardiac phase in this chapter, which may not be an optimum choice. The proposed method reconstructs each cardiac phase image independently and the temporal domain does not require a specific undersampling pattern for the CS reconstruction.

It is shown that utilizing the fully-sampled FB images is effective to sparsify the difference images in radial acquisition. It is well-known that radial acquisition has superior performance with respect to object motion compared with Cartesian acquisition [82, 83]. While the standard two-dimensional Cartesian acquisition spreads the motion artifacts mainly in the phase-encoding direction resulting in a severe ghosting artifact in that direction, the radial acquisition changes the phase-encoding direction over the entire two-dimensional space and the motion artifacts appear as two-dimensional blurring and streaks which are less objectionable and of lower intensity. We have observed blurred images from the fully-sampled FB acquisitions in most of our cases, but the streaking artifacts were not significant as shown in Figure 4.2. Using Cartesian trajectory may not be suitable for the proposed CS reconstruction since the difference images from the FB images may not be sparse enough for the successful CS reconstruction due to the severe motion artifact in the fully-sampled FB images.

The proposed acquisition strategy does not increase the total scan time because the auxiliary FB acquisition is acquired during the resting period which has not been used for acquiring data conventionally. The proposed CS reconstruction allows undersampling of the BH acquisition by a factor of three to five without severely degrading the quality of the cine images. As the undersampling factor increases, the

BH duration is reduced accordingly. It is also possible to acquire undersampled data for multiple slices in one BH.

4.4 Conclusion

The data acquired during rest period between multiple BHs of cine MRI can be used to improve the image reconstruction of accelerated radial cine MRI without increasing the total scan time.

Chapter 5

Respiratory Motion Correction Using Compressed Sensing Reconstruction for Whole-Heart MRI with 3D Radial Trajectory

In Chapter 2, we have mentioned that 3D acquisition of the whole-heart image has many advantages over 2D acquisition: simple image prescription, large coverage, superior through-plane spatial resolution, higher SNR, easy reformatting of the image in any desired plane, etc. It is also mentioned that the prolonged data acquisition time is one of the major disadvantage of the 3D acquisition. For whole-heart coronary MRI, the acquisition time becomes even longer in order to compensate for the respiratory motion and the cardiac motion. To image the coronary arteries correctly without the cardiac motion, electrocardiography (ECG) signal is commonly used to monitor the cardiac activity over a period of time. The MR data is acquired only in a short interval around 100 ms during the "quiescent" time in the mid-diastole window within the cardiac cycle (rest period) [92]. In the rest period, the coronary arteries remain relatively still, and the acquisition during the rest period over multiple cardiac cycles will fill the entire k-space resulting in a cardiac motion-free image.

The respiratory motion can be compensated by various methods. The simplest way is to acquire the data during patient holding his/her breath. Breath-hold (BH) acquisitions have been commonly used in cardiac cine imaging as discussed in Chapter 4. BH acquisition have been also used for coronary MRIs [93, 94]. Due to the limited duration of BH acquisition and due to the inconsistency in the heart position among different BHs, it is not well-suited for 3D acquisition with large FOV and high spatial resolution. Respiratory gating with the respiratory navigator (NAV) signal is most commonly used for free breathing acquisitions to freeze the respiratory motion of the object [59, 95, 96, 97]. It is shown that the motion of the heart is approximately linearly related with the superior-inferior (SI) motion of the diaphragm [98, 99] with an average correlation factor of 0.6, although highly patient specific. A 2D spiral selective RF pulse, which consists of an RF waveform followed by 2D gradient waveforms, is located on the dome of the right hemidiaphragm to extract the motion of diaphragm. The k-space data acquisition is performed immediately after the NAV signal. If the NAV signal is within a certain predefined window (gating window), the acquired k-space lines are accepted. If the NAV signal is outside the gating window, the acquired k-space lines are rejected, and the scanner tries to re-acquire the rejected k-space lines in the subsequent heart beats until the NAV signal falls into the gating window. A gating window of 5 mm to 7 mm is commonly used, which yields an acceptance ratio of 30-80%. The acceptance ratio is also patient-specific, unpredictable and results in an increased acquisition time by 1.5-3 times compared with non-gated acquisition.

Self-navigated motion detection/correction methods have also been developed [63, 100, 101]. In self-navigated methods, a low resolution image of the entire heart or a projection data along SI direction is extracted from the acquired k-space data, and the respiratory motion is compensated by using this information. In [63], the 3D radial trajectory is slightly modified to have the first projection line acquired in each heart beat would be oriented in the SI direction, and the respiratory motion is corrected by modulating the k-space lines in each cardiac cycle with a linear phase shift according to the Fourier shift theorem.

Compressed sensing motion correction (CosMo) [102] has been presented for free-breathing coronary MRI with Cartesian acquisition in order to reduce the scan time of NAV gated acquisition. The respiratory NAV signal is acquired but only utilized to determine the acceptance/rejection of the acquired k-space line retrospectively. The resulting k-space data only contains motion-free k-space lines acquired within the acceptance window, but the data is undersampled due to the rejected k-space lines. The rejected k-space lines are estimated by the CS reconstruction, resulting in motion-free image. In this chapter, we propose to use similar technique for the reconstruction of 3D radial acquisition to mitigate the effect of respiratory motion in free-breathing whole-heart acquisition and evaluate the efficacy of the proposed respiratory motion correction technique with healthy volunteer study.

5.1 Materials and Methods

5.1.1 Original CosMo Acquisition

The CosMo data acquisition procedure with Cartesian trajectory consists of two different strategies for the inner k-space region and outer k-space region. The inner k-space region is fully sampled using a conventional prospective diaphragmatic navigator with a predefined acceptance window with re-acquisition of the discarded k-space lines to guarantee motion-free acquisition of the inner k-space region. The outer k-space region is also acquired with the NAV signal, but a wider acceptance window of 100 mm is used to accept all the acquired k-space lines. The recorded NAV signal is used to retrospectively select the motion-free k-space lines within the acceptance window which will be included in the CS reconstruction. If the recorded NAV signal lies outside of the acceptance window, the corresponding k-space line is considered as respiratory motion-corrupted, and is excluded from the reconstruction without re-acquisition. The CS reconstruction is performed only using the fully-sampled inner k-space region and the motion-free k-space lines in the outer k-space region, and the respiratory motion is corrected without re-acquiring the missing k-space data. We note that the inner k-space region, i.e., the central portion of the k-space, is fully acquired as the center of the k-space contains the majority of the signal of the underlying object.

5.1.2 Proposed Acquisition with 3D Radial Trajectory and CS Reconstruction

The 3D radial sampling trajectory introduced in Chapter 2 was used in this chapter. A diaphragmatic navigator is placed on the dome of right hemidiaphragm to monitor the respiratory motion. The NAV signals acquired during the preparation phase are used to determine the reference position of the hemidiaphragm. A standard NAV gating method with re-acquisition was used but an acceptance window of 100 mm was used to accept all the acquired k-space lines regardless of their NAV position. The recorded NAV signal and the k-space data were transferred to a stand-alone personal computer for retrospective gating and the CS reconstruction.

The acquired k-space data $\mathbf{y}$ and the desired image $\mathbf{x}$ are formulated as an encoding matrix format as $\mathbf{y} = \mathbf{A}\mathbf{x}$, where $\mathbf{A}$ denotes the encoding matrix. As in the previous chapters, the 3D image is represented in a single column vector for mathematical convenience. Among all the k-space lines in the 3D radial trajectory, the motion-free k-space lines within the gating window are denoted as $\mathbf{y}_\Omega = \mathbf{A}_\Omega \mathbf{x}$, where Ω is the index set of the motion-free k-space lines and $\mathbf{A}_\Omega$ denotes the matrix whose columns are selected as the subset Ω of the columns of $\mathbf{A}$. The matrix $\mathbf{A}$ performs the de-apodization, Fourier transform and the gridding operation as described in Chapter 2. The CS reconstruction solves the minimization problem using the motion-free k-space lines only:

$$\arg\min_{\mathbf{x}} \frac{1}{2}||\mathbf{A}_\Omega x - \mathbf{y}_\Omega||_2^2 + \lambda||\mathbf{\Psi}\mathbf{x}||_1, \tag{5.1}$$

where λ is a regularization parameter which determines the tradeoff between the data consistency and the sparsity level of the image and $\mathbf{\Psi}$ is a sparsifying transform matrix. The two-stage iterative method consisting of *data consistency step* and *thresholing step* described in the previous chapters was utilized to solve the CS reconstruction problem.

5.1.3 In Vivo Study

Whole-heart coronary MR images were acquired on 7 healthy volunteers (3 male, 29±13 years). 3D free-breathing ECG-triggered SSFP sequences were used for imaging the heart with 3D radial trajectories. A respiratory navigator with 100 mm gating window was used to track the right hemidiaphragm position and recorded for retrospective gating. The data sets were acquired with $N_s = 392$ samples per projection line and $N_i = 10$ total interleaves for sampling densities of 30%. The scan parameters used for this study were as follows: TR/TE/α = 3.20/1.61/90°, FOV = $260 \times 260 \times 260\ mm^3$, spatial resolution = $1.4 \times 1.4 \times 1.4\ mm^3$. The nominal scan time for the data set with sampling density of 30% was reported to be 169 seconds assuming 100% navigator gating efficiency.

The acquired 3D radial data were reconstructed by three reconstruction methods: conventional gridding reconstruction is performed on the free-breathing data sets containing all the motion-free and motion-corrupted k-space lines (with 100% gating efficiency), conventional gridding reconstruction is performed on the data sets with motion-free k-space lines only (with 5 mm retrospective gating window), and the proposed motion correction method using the CS reconstruction on the data sets with motion-free k-space lines only.

5.1.4 Data Analysis

For quantitative assessment of the quality of the proposed motion correction method, the vessel sharpness and the vessel length of the right coronary artery (RCA) were measured using Soap-Bubble software [60]. The sharpness score and the length of the vessels with the proposed method were compared with those of the conventional gridding reconstruction algorithm using a paired t-test. A value of $P < 0.05$ was considered to be statistically significant.

5.2 Results

Figures 5.1 and 5.2 show example slices of axial and reformatted sagittal views from 3D whole-heart images with isotropic 1.4 mm spatial resolution with different reconstructions: conventional gridding reconstruction with free-breathing dataset, conventional gridding reconstruction with retrospectively gated dataset, and CS motion correction reconstruction with retrospectively gate dataset. The sampling density of the free-breathing dataset is 30%. The retrospectively gated data was generated from the same free-breathing dataset with 5 mm gating window, resulting in an average effective sampling density of 18.18% over four volunteer datasets.

The images reconstructed from the free-breathing dataset present aliasing artifacts and blurring due to the respiratory motion. The images reconstructed from retrospectively gated dataset appear sharper, but exhibits streaking artifacts due to the retrospective undersampling. The CS motion correction reconstruction provides the sharpest image qualities among the three reconstruction methods. The streaking artifacts are substantially suppressed and the blood pool appears clearer and more homogeneous compared to other reconstruction methods.

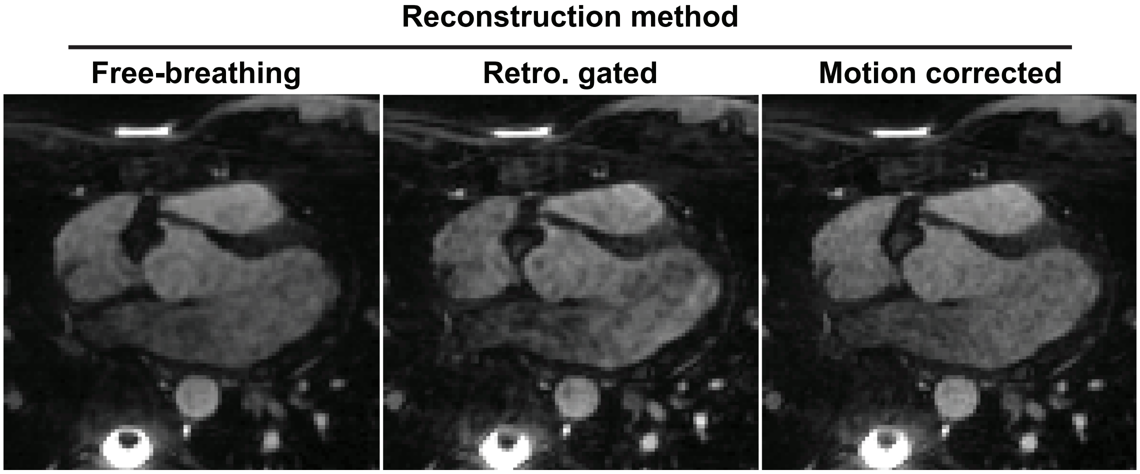

Figure 5.1: Example slices sagittal views from 3D whole-heart images reconstructed by conventional 3D gridding reconstruction and iterative CS reconstruction (with 1000 iterations for image domain regularization and 500 iterations for wavelet domain regularization) for different sampling densities. For all the sampling densities, CS reconstructions have less high-frequency streaking artifacts, and the improvement in the image quality is more distinct at lower sampling densities.

Table 5.1 summarizes the vessel quantitative measurement results of the 3D whole-heart images from 7 volunteer datasets with sampling densities of 30%. The CS motion correction improves both the vessel length and the vessel sharpness. The RCA length was increased by 34% and the RCA sharpness was improved by 12% compared with free-breathing data without any motion correction. The increase in vessel length is statistically significant between the free-breathing image and the motion corrected image. The increase in RCA sharpness of the motion corrected image is also significantly different from that of the free-breathing image.

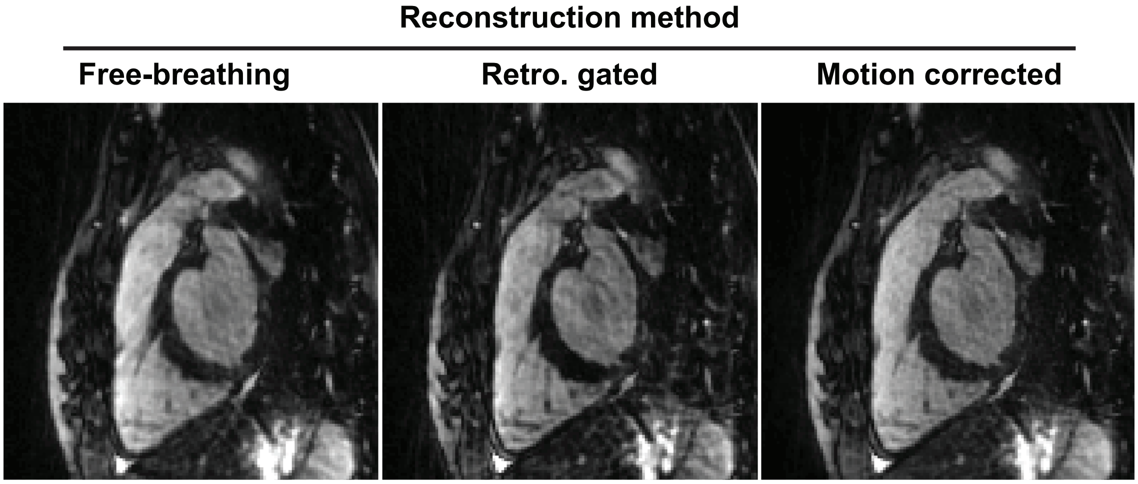

Figure 5.2: Example slices sagittal views from 3D whole-heart images reconstructed by conventional 3D gridding reconstruction and iterative CS reconstruction (with 1000 iterations for image domain regularization and 500 iterations for wavelet domain regularization) for different sampling densities. For all the sampling densities, CS reconstructions have less high-frequency streaking artifacts, and the improvement in the image quality is more distinct at lower sampling densities.

Reconstruction method	RCA length (cm)	RCA sharpnes
Free-breathing	$5.28 \pm 1.87^*$	$0.41 \pm 0.06^*$
Retrospective gating	6.67 ± 1.67	0.42 ± 0.08
Motioned corrected	7.11 ± 1.81	0.46 ± 0.09

Table 5.1: Mean ± standard deviation of normalized vessel sharpness and vessel length (cm) measured for free-breathing data with gridding reconstruction, retrospectively gated data with gridding reconstruction and retrospectively gate data with CS motion correction. (*: $P < 0.05$ compared with motion corrected image)

5.3 Discussion

In this chapter, we have evaluated the feasibility of using CS to correct the respiratory motion of free-breathing 3D whole-heart coronary MRI acquisition. Unlike the Cartesian trajectory, every k-space line in radial trajectory pass through the origin of k-space and thus has equal amount of significance in average, thus does not require two separate acquisition strategies for inner and outer k-space lines as in original CosMo acquisition with Cartesian trajectory [102]. Although the original CosMo acquisition with Cartesian trajectory provides a good estimation on the total scan time, the actual scan time may not be estimated with high accuracy due to the prospectively gated acquisition of the inner k-space region. The scan time increases and also becomes less predictable as the portion of inner k-space region increases over the entire k-space. The proposed motion correction with 3D radial trajectory provide a truly fixed scan time independent of the patient's breathing pattern and allow the planning of the entire scanning procedure to be more predictable. In this chapter, we used the diaphragmatic NAV to monitor the respiratory motion. It is only used to accept/reject the k-space lines according to the predefined retrospective gating window. Conventional self-gating motion correction technique such as [63] utilizes the projection data along SI direction. The SI motion is extracted from the projection data, and the motion is compensated on the corresponding motion-corrupted k-space lines according to the Fourier shift theorem. Thus the self-gated technique is limited to correct one dimensional rigid motion along the SI direction. The proposed CS motion correction is not limited to correct one dimensional motion because it does not explicitly correct the motion on the motion-corrupted data but indirectly estimate the motion by CS reconstruction. The proposed method may potentially correct complex multi-dimensional motions including non-rigid motions although it has not been shown in this chapter.

5.4 Conclusion

We have implemented a motion correction technique by using compressed sensing reconstruction for 3D radial acquisition, and evaluated its performance to correct the respiratory motion in free-breathing 3D whole-heart coronary MRI. The proposed motion correction technique successfully suppressed motion-induced artifacts and improved the image quality of free-breathing undersampled 3D radial data sets compared to the conventional gridding reconstruction without any motion correction, thus allowing reduced acquisition time compared with prospective NAV gated acquisition.

Bibliography

[1] JPEG standard, ITU-T T.81, ISO/IEC 10918-1.

[2] JPEG2000 standard, ITU-T T.800, ISO/IEC 15444-1.

[3] D. L. Donoho. Compressed sensing. *IEEE Trans. on Inf. Theory*, 52(4):1289–1306, April 2006.

[4] E. J. Candès, J. Romberg, and T. Tao. Robust uncertainty principles: exact signal reconstruction from highly incomplete frequency information. *IEEE Trans. on Inf. Theory*, 52:489–509, February 2006.

[5] B. K. Natarajan. Sparse approximate solutions to linear systems. *SIAM J. Comput.*, 24:227–234, 1995.

[6] E. J. Candès and T. Tao. Decoding by linear programming. *IEEE Trans. on Inf. Theory*, 51(12):4203–4215, December 2005.

[7] D. L. Donoho and J. Tanner. Counting faces of randomly projected polytopes when the projection radically lowers dimension. *J. Amer. Math. Soc.*, 22(1):1–53, 2009.

[8] D.L. Donoho and X. Huo. Uncertainty principles and ideal atomic decomposition. *Information Theory, IEEE Transactions on*, 47(7):2845 –2862, nov 2001.

[9] J.-J. Fuchs. On sparse representations in arbitrary redundant bases. *Information Theory, IEEE Transactions on*, 50(6):1341 – 1344, june 2004.

[10] M. Elad and A.M. Bruckstein. A generalized uncertainty principle and sparse representation in pairs of bases. *Information Theory, IEEE Transactions on*, 48(9):2558 – 2567, sep 2002.

[11] J. A. Tropp. Greed is good: Algorithmic results for sparse approximation. *IEEE Trans. on Inf. Theory*, 50(10):2231–2242, October 2004.

[12] J.A. Tropp. Just relax: convex programming methods for identifying sparse signals in noise. *Information Theory, IEEE Transactions on*, 52(3):1030 –1051, march 2006.

[13] E. J. Candès, J. Romberg, and T. Tao. Stable signal recovery for incomplete and inaccurate measurements. *Commun. Pure Appl. Math*, 59:1207–1223, August 2006.

[14] E. J. Candès and P. A. Randall. Highly robust error correction by convex programming. *IEEE Trans. on Inf. Theory*, 54(7):2829–2840, July 2008.

[15] E. J. Candès and J. Romberg. Practical signal recovery from random projections. In *Proc. Wavelet Appl. Signal Image Process. XI, SPIE Conf.*, 2005.

[16] M. A. T. Figueiredo and R. Nowak. An EM algorithm for wavelet-based image restoration. *IEEE Trans. Image Proc.*, 12:906–916, August 2003.

[17] M. A. T. Figueiredo, R. Nowak, and S. J. Wright. Gradient projection for sparse reconstruction: Application to compressed sensing and other inverse problems. *IEEE Journal of Selected Topics in Signal Processing*, 1:586–598, December 2007.

[18] J. A. Tropp. *Topics in Sparse Approximation.* PhD thesis, UT-Austin, August 2004.

[19] E. van den Berg and M. P. Friedlander. Necessary and sufficient conditions on sparsity pattern recovery. *SIAM J. Sci. Comput.*, 31(2):890–912, 2008.

[20] M. J. Wainwright. Sharp thresholds for noisy and high-dimensional recovery of sparsity using ℓ_1-constrained quadratic programming (lasso). *IEEE Trans. on Inf. Theory*, 55(5):2183–2202, May 2009.

[21] E. J. Candès and J. Romberg. Sparsity and incoherence in compressive sampling. *Inverse Problems*, 23(3):969–985, 2007.

[22] O. M. Weber, A. J. Martin, and C. B. Higgins. Whole-heart steady-state free precession coronary artery magnetic resonance angiography. *Magn Reson Med*, 50(6):1223–8, 2003.

[23] K. Nehrke, P. Bornert, P. Mazurkewitz, R. Winkelmann, and I. Graß lin. Free-breathing whole-heart coronary MR angiography on a clinical scanner in four minutes. *Journal of Magnetic Resonance Imaging*, 23(5):752–756, 2006.

[24] X. Bi, J. C. Carr, and D. Li. Whole-heart coronary magnetic resonance angiography at 3 Tesla in 5 minutes with slow infusion of Gd-BOPTA, a high-relaxivity clinical contrast agent. *Magn Reson Med*, 58(1):1–7, 2007.

[25] M. T. Alley, S. Napel, Y. Amano, D. S. Paik, R. Y. Shifrin, A. Shimakawa, N. J. Pelc, and R. J. Herfkens. Fast 3D cardiac cine MR imaging. *J Magn Reson Imaging*, 9(5):751–5, 1999.

[26] A. V. Barger, T. M. Grist, W. F. Block, and C. A. Mistretta. Single breath-hold 3D contrast-enhanced method for assessment of cardiac function. *Magn Reson Med*, 44(6):821–4, 2000.

[27] S. Kozerke, J. Tsao, R. Razavi, and P. Boesiger. Accelerating cardiac cine 3D imaging using k-t BLAST. *Magn Reson Med*, 52(1):19–26, 2004.

[28] T. D. Nguyen, P. Spincemaille, J. W. Weinsaft, B. Y. Ho, M. D. Cham, M. R. Prince, and Y. Wang. A fast navigator-gated 3D sequence for delayed enhancement MRI of the myocardium: Comparison with breathhold 2D imaging. *J Magn Reson Imaging*, 27(4):802–8, 2008.

[29] D. C. Peters, E. A. Appelbaum, R. Nezafat, B. Dokhan, Y. Han, K. V. Kissinger, B. Goddu, and W. J. Manning. Left ventricular infarct size, peri-infarct zone, and papillary scar measurements: A comparison of high-resolution 3D and conventional 2D late Gadolinium enhancement cardiac MR. *J Magn Reson Imaging*, 30(4):794–800, 2009.

[30] T. Shin, H. H. Hu, G. M. Pohost, and K. S. Nayak. Three dimensional first-pass myocardial perfusion imaging at 3T: Feasibility study. *J Cardiovasc Magn Reson*, 10:57, 2008.

[31] R. Otazo, J. Xu, L. Axel, and D. Sodickson. Combination of compressed sensing and parallel imaging for highly-accelerated 3D first-pass cardiac perfusion MRI. In *Proceedings of the 18th Scientific Meeting of ISMRM*, page 344, Stockholm, 2010.

[32] D. C. Peters, F. R. Korosec, T. M. Grist, W. F. Block, J. E. Holden, K. K. Vigen, and C. A. Mistretta. Undersampled projection reconstruction applied to mr angiography. *Magnetic Resonance in Medicine*, 43(1):91–101, 2000.

[33] D. R. Thedens, P. Irarrazaval, T. S. Sachs, C. H. Meyer, and D. G. Nishimura. Fast magnetic resonance coronary angiography with a three-dimensional stack of spirals trajectory. *Magnetic Resonance in Medicine*, 41(6):1170–1179, 1999.

[34] H. Bhat, Q. Yang, S. Zuehlsdorff, K. Li, and D. Li. Contrast-enhanced whole-heart coronary magnetic resonance angiography at 3T with radial EPI. *Magnetic Resonance in Medicine*, pages 82–91, 2011.

[35] H. Bhat, L. Ge, S. Nielles-Vallespin, S. Zuehlsdorff, and D. Li. 3D radial sampling and 3D affine transform-based respiratory motion correction technique for free-breathing whole-heart coronary MRA with 100% imaging efficiency. *Magnetic Resonance in Medicine*, 65(5):1269–1277, 2011.

[36] C. Stehning, P. Bornert, K. Nehrke, H. Eggers, and O. Dossel. Fast isotropic volumetric coronary MR angiography using free-breathing 3D radial balanced FFE acquisition. *Magnetic Resonance in Medicine*, 52(1):197–203, 2004.

[37] A. V. Barger, W. F. Block, Y. Toropov, T. M. Grist, and C. A. Mistretta. Time-resolved contrast-enhanced imaging with isotropic resolution and broad coverage using an undersampled 3D projection trajectory. *Magnetic Resonance in Medicine*, 48(2):297–305, 2002.

[38] P. Lai, F. Huang, Y. Li, S. Nielles-Vallespin, X. Bi, R. Jerecic, and D. Li. Contrast-kinetics-resolved whole-heart coronary MRA using 3DPR. *Magnetic Resonance in Medicine*, 63(4):970–978, 2010.

[39] T. Gu, F. R. Korosec, W. F. Block, S. B. Fain, Q. Turk, D. Lum, Y. Zhou, T. M. Grist, V. Haughton, and C. A. Mistretta. PC VIPR: A high-speed 3D phase-contrast method for flow quantification and high-resolution angiography. *AJNR Am J Neuroradiol*, 26(4):743–749, 2005.

[40] J. D. O'Sullivan. A fast sinc function gridding algorithm for fourier inversion in computer tomography. *Medical Imaging, IEEE Transactions on*, 4(4):200–207, 1985.

[41] K. T. Block, M. Uecker, and J. Frahm. Undersampled radial MRI with multiple coils. iterative image reconstruction using a total variation constraint. *Magnetic Resonance in Medicine*, 57(6):1086–1098, 2007.

[42] K. P. Pruessmann, M. Weiger, M. B. Scheidegger, and P. Boesiger. SENSE: Sensitivity encoding for fast MRI. *Magnetic Resonance in Medicine*, 42(5):952–962, 1999.

[43] M. A. Griswold, P. M. Jakob, R. M. Heidemann, M. Nittka, V. Jellus, J. Wang, B. Kiefer, and A. Haase. Generalized autocalibrating partially parallel acquisitions (GRAPPA). *Magnetic Resonance in Medicine*, 47(6):1202–1210, 2002.

[44] K. P. Pruessmann, M. Weiger, P. Bornert, and P. Boesiger. Advances in sensitivity encoding with arbitrary k-space trajectories. *Magnetic Resonance in Medicine*, 46(4):638–651, 2001.

[45] N. Seiberlich, F. A. Breuer, M. Blaimer, K. Barkauskas, P. M. Jakob, and M. A. Griswold. Non-Cartesian data reconstruction using GRAPPA operator gridding (GROG). *Magnetic Resonance in Medicine*, 58(6):1257–1265, 2007.

[46] T. C. Chang, L. He, and T. Fang. Mr image reconstruction from sparse radial samples using Bregman iteration. In *Proceedings of the 13th Scientfic Meeting of ISMRM*, page 696, Seattle, 2006.

[47] A. Beck and M. Teboulle. A fast iterative shrinkage-thresholding algorithm for linear inverse problems. *SIAM Journal on Imaging Sciences*, 2(1):183–202, 2009.

[48] S. T. S. Wong and M. S. Roos. A strategy for sampling on a sphere applied to 3D selective RF pulse design. *Magnetic Resonance in Medicine*, 32(6):778–784, 1994.

[49] J. G. Pipe and P. Menon. Sampling density compensation in MRI: Rationale and an iterative numerical solution. *Magnetic Resonance in Medicine*, 41(1):179–186, 1999.

[50] K. O. Johnson and J. G. Pipe. Convolution kernel design and efficient algorithm for sampling density correction. *Magn Reson Med*, 61(2):439–47, 2009.

[51] N. R. Zwart, K. O. Johnson, and J. G. Pipe. Efficient sample density estimation by combining gridding and an optimized kernel. *Magn Reson Med*, 2011.

[52] M. A. Brown and R. C. Semelka. *MRI Basic Principles and Applications*. John Wiley and Sons, Inc., Hoboken, New Jersey, 3rd edition, 2003.

[53] V. Rasche, R. Proksa, R. Sinkus, P. Bornert, and H. Eggers. Resampling of data between arbitrary grids using convolution interpolation. *Medical Imaging, IEEE Transactions on*, 18(5):385–392, 1999.

[54] I. Daubechies, M. Defries, and C. De Mol. An iterative thresholding algorithm for linear inverse problems with a sparsity constraint. *Communications on Pure and Applied Mathematics*, 57:1413–1457, 2004.

[55] S. J. Wright, R. D. Nowak, and M. A. T. Figueiredo. Sparse reconstruction by separable approximation. *Signal Processing, IEEE Transactions on*, 57(7):2479–2493, 2009.

[56] I. Daubechies. *Ten lectures on wavelets*. Society for Industrial and Applied Mathematics, Philadelphia, PA, 1992.

[57] Seung-Jean Kim, K. Koh, M. Lustig, S. Boyd, and D. Gorinevsky. An interior-point method for large-scale l1-regularized least squares. *Selected Topics in Signal Processing, IEEE Journal of*, 1(4):606 –617, dec. 2007.

[58] J. I. Jackson, C. H. Meyer, D. G. Nishimura, and A. Macovski. Selection of a convolution function for Fourier inversion using gridding (computerised tomography application). *Medical Imaging, IEEE Transactions on*, 10(3):473–478, 1991.

[59] A. D. Scott, J. Keegan, and D. N. Firmin. Motion in cardiovascular MR imaging. *Radiology*, 250(2):331–51, 2009.

[60] A. Etienne, R. M. Botnar, A. M. C. van Muiswinkel, P. Boesiger, W. J. Manning, and M. Stuber. Soap-Bubble visualization and quantitative analysis of 3D coronary magnetic resonance angiograms. *Magnetic Resonance in Medicine*, 48(4):658–666, 2002.

[61] R. Deriche. Fast algorithms for low-level vision. *IEEE Trans. Pattern Anal. Mach. Intell.*, 12(1):78–87, 1990.

[62] R. M. Botnar, M. Stuber, P. G. Danias, K. V. Kissinger, and W. J. Manning. Improved coronary artery definition with T2-weighted, free-breathing, three-dimensional coronary MRA. *Circulation*, 99(24):3139–48, 1999.

[63] C. Stehning, P. Bornert, K. Nehrke, H. Eggers, and M. Stuber. Free-breathing whole-heart coronary MRA with 3D radial SSFP and self-navigated image reconstruction. *Magnetic Resonance in Medicine*, 54(2):476–480, 2005.

[64] M. Lustig, D. Donoho, and J. M. Pauly. Sparse MRI: The application of compressed sensing for rapid MR imaging. *Magnetic Resonance in Medicine*, 58(6):1182–1195, 2007.

[65] M. Lustig and J. M. Pauly. SPIRiT: Iterative self-consistent parallel imaging reconstruction from arbitrary k-space. *Magn Reson Med*, 64(2):457–71, 2010.

[66] T. Çukur, M. Lustig, and D. G. Nishimura. Improving non-contrast-enhanced steady-state free precession angiography with compressed sensing. *Magnetic Resonance in Medicine*, 61(5):1122–1131, 2009.

[67] M. Akcakaya, P. Hu, M. L. Chuang, T. H. Hauser, L. H. Ngo, W. J. Manning, V. Tarokh, and R. Nezafat. Accelerated noncontrast-enhanced pulmonary vein MRA with distributed compressed sensing. *J Magn Reson Imaging*, 33(5):1248–55, 2011.

[68] M. Doneva, P. Bornert, H. Eggers, C. Stehning, J. Senegas, and A. Mertins. Compressed sensing reconstruction for magnetic resonance parameter mapping. *Magn Reson Med*, 64(4):1114–20, 2010.

[69] M. Akcakaya, T. A. Basha, B. Goddu, L. A. Goepfert, K. V. Kissinger, V. Tarokh, W. J. Manning, and R. Nezafat. Low-dimensional-structure self-learning and thresholding: Regularization beyond compressed sensing for MRI reconstruction. *Magn Reson Med*, 66(3):756–67, 2011.

[70] T. S. Sorensen, T. Schaeffter, K. O. Noe, and M. S. Hansen. Accelerating the nonequispaced fast Fourier transform on commodity graphics hardware. *Medical Imaging, IEEE Transactions on*, 27(4):538–547, 2008.

[71] T. S. Sorensen, D. Atkinson, T. Schaeffter, and M. S. Hansen. Real-time reconstruction of sensitivity encoded radial magnetic resonance imaging using a graphics processing unit. *Medical Imaging, IEEE Transactions on*, 28(12):1974–1985, 2009.

[72] F. Knoll, M. Unger, C. Diwoky, C. Clason, T. Pock, and R. Stollberger. Fast reduction of undersampling artifacts in radial MR angiography with 3D total variation on graphics hardware. *Magnetic Resonance Materials in Physics, Biology and Medicine*, 23(2):103–114, 2010.

[73] G. Buchgraber, F. Knoll, M. Freiberger, C. Clason, M. Grabner, and R. Stollberger. Fast regridding using LSQR on graphics hardware. In *Proceedings of the 18th Scientfic Meeting of ISMRM*, page 4959, Stockholm, 2010.

[74] S. S. Stone, J. P. Haldar, S. C. Tsao, W. m W. Hwu, B. P. Sutton, and Z. P. Liang. Accelerating advanced MRI reconstructions on GPUs. *Journal of Parallel and Distributed Computing*, 68(10):1307–1318, 2008.

[75] Nvidia. Nvidia's next generation CUDA compute architecture: Fermi. white paper. white paper, NVIDIA Corporation, 2009.

[76] Bruno Madore, Gary H. Glover, and Norbert J. Pelc. Unaliasing by fourier-encoding the overlaps using the temporal dimension (unfold), applied to cardiac imaging and fmri. *Magnetic Resonance in Medicine*, 42(5):813–828, 1999.

[77] Peter Kellman, Frederick H. Epstein, and Elliot R. McVeigh. Adaptive sensitivity encoding incorporating temporal filtering (TSENSE). *Magnetic Resonance in Medicine*, 45(5):846–852, 2001.

[78] J. Tsao, P. Boesiger, and K. P. Pruessmann. k-t BLAST and k-t SENSE: dynamic MRI with high frame rate exploiting spatiotemporal correlations. *Magn Reson Med*, 50(5):1031–42, 2003.

[79] U. Gamper, P. Boesiger, and S. Kozerke. Compressed sensing in dynamic MRI. *Magnetic Resonance in Medicine*, 59(2):365–373, 2008.

[80] P. C. Lauterbur. Image formation by induced local interactions: Examples employing nuclear magnetic resonance. *Nature*, 242(5394):190–191, 1973. 10.1038/242190a0.

[81] G. H. Glover and J. M. Pauly. Projection reconstruction techniques for reduction of motion effects in MRI. *Magnetic Resonance in Medicine*, 28(2):275–289, 1992.

[82] T. P. Trouard, Y. Sabharwal, M. I. Altbach, and A. F. Gmitro. Analysis and comparison of motion-correction techniques in diffusion-weighted imaging. *J Magn Reson Imaging*, 6(6):925–35, 1996.

[83] M. Katoh, E. Spuentrup, A. Buecker, W. J. Manning, R. W. Gunther, and R. M. Botnar. Mr coronary vessel wall imaging: comparison between radial and spiral k-space sampling. *J Magn Reson Imaging*, 23(5):757–62, 2006.

[84] A. Shankaranarayanan, O. P. Simonetti, G. Laub, J. S. Lewin, and J. L. Duerk. Segmented k-space and real-time cardiac cine mr imaging with radial trajectories. *Radiology*, 221(3):827–36, 2001.

[85] J. C. Ye, S. Tak, Y. Han, and H. W. Park. Projection reconstruction mr imaging using focuss. *Magn Reson Med*, 57(4):764–75, 2007.

[86] N. Seiberlich, F. Breuer, R. Heidemann, M. Blaimer, M. Griswold, and P. Jakob. Reconstruction of undersampled non-cartesian data sets using pseudo-cartesian grappa in conjunction with grog. *Magn Reson Med*, 59(5):1127–37, 2008.

[87] M. S. Hansen, C. Baltes, J. Tsao, S. Kozerke, K. P. Pruessmann, and H. Eggers. k-t blast reconstruction from non-cartesian k-t space sampling. *Magn Reson Med*, 55(1):85–91, 2006.

[88] H. Jung, J. Park, J. Yoo, and J. C. Ye. Radial k-t focuss for high-resolution cardiac cine mri. *Magn Reson Med*, 63(1):68–78, 2010.

[89] Rachel W. Chan, Elizabeth A. Ramsay, Edward Y. Cheung, and Donald B. Plewes. The influence of radial undersampling schemes on compressed sensing reconstruction in breast mri. *Magnetic Resonance in Medicine*, 67(2):363–377, 2012.

[90] A. C. Larson, P. Kellman, A. Arai, G. A. Hirsch, E. McVeigh, D. Li, and O. P. Simonetti. Preliminary investigation of respiratory self-gating for free-breathing segmented cine mri. *Magn Reson Med*, 53(1):159–168, 2005.

[91] Urs Gamper, Peter Boesiger, and Sebastian Kozerke. Compressed sensing in dynamic mri. *Magnetic Resonance in Medicine*, 59(2):365–373, 2008.

[92] Y. Wang, E. Vidan, and G. W. Bergman. Cardiac motion of coronary arteries: variability in the rest period and implications for coronary mr angiography. *Radiology*, 213(3):751–8, 1999.

[93] R. R. Edelman, W. J. Manning, D. Burstein, and S. Paulin. Coronary arteries: breath-hold mr angiography. *Radiology*, 181(3):641–3, 1991.

[94] T. Niendorf, C. J. Hardy, R. O. Giaquinto, P. Gross, H. E. Cline, Y. Zhu, G. Kenwood, S. Cohen, A. K. Grant, S. Joshi, N. M. Rofsky, and D. K. Sodickson. Toward single breath-hold whole-heart coverage coronary mra using highly accelerated parallel imaging with a 32-channel mr system. *Magn Reson Med*, 56(1):167–76, 2006.

[95] R. L. Ehman and J. P. Felmlee. Adaptive technique for high-definition mr imaging of moving structures. *Radiology*, 173(1):255–63, 1989.

[96] Y. Wang, P. J. Rossman, R. C. Grimm, S. J. Riederer, and R. L. Ehman. Navigator-echo-based real-time respiratory gating and triggering for reduction of respiration effects in three-dimensional coronary mr angiography. *Radiology*, 198(1):55–60, 1996.

[97] A. M. Taylor, P. Jhooti, F. Wiesmann, J. Keegan, D. N. Firmin, and D. J. Pennell. Mr navigator-echo monitoring of temporal changes in diaphragm position: implications for mr coronary angiography. *J Magn Reson Imaging*, 7(4):629–36, 1997.

[98] Y. Wang, S. J. Riederer, and R. L. Ehman. Respiratory motion of the heart: kinematics and the implications for the spatial resolution in coronary imaging. *Magn Reson Med*, 33(5):713–9, 1995.

[99] K. Nehrke, P. Bornert, D. Manke, and J. C. Bock. Free-breathing cardiac mr imaging: study of implications of respiratory motion–initial results. *Radiology*, 220(3):810–5, 2001.

[100] J. G. Pipe. Motion correction with propeller mri: application to head motion and free-breathing cardiac imaging. *Magn Reson Med*, 42(5):963–9, 1999.

[101] P. Lai, X. Bi, R. Jerecic, and D. Li. A respiratory self-gating technique with 3d-translation compensation for free-breathing whole-heart coronary mra. *Magn Reson Med*, 62(3):731–8, 2009.

[102] Mehdi H. Moghari, Mehmet Akakaya, Alan O'Connor, Tamer A. Basha, Michele Casanova, Douglas Stanton, Lois Goepfert, Kraig V. Kissinger, Beth Goddu, Michael L. Chuang, Vahid Tarokh, Warren J. Manning, and Reza Nezafat. Compressed-sensing motion compensation (CosMo): A joint prospective retrospective respiratory navigator for coronary mri. *Magnetic Resonance in Medicine*, 66(6):1674–1681, 2011.

Glossary of Abbreviations

BH	breath-hold
CMR	cardiac magnetic resonance
CS	compressed sensing
CUDA	compute unified device architecture
DCF	density compensation function
DWT	discrete wavelet transform
ECG	electrocardiography
FB	free-breathing
FFT	fast Fourier transform
FOV	field of view
GPU	graphics processing unit
HLA	horizontal long axis
LGE	late Gadolinium enhancement
LV	left ventricle
LVEF	left ventricle ejection fraction
LVEDV	left ventricle end-diastolic volume
LVESV	left ventricle end-systolic volume
MRI	magnetic resonance imaging
MSE	mean-squared error
NAV	navigator
NUFFT	nonuniform fast Fourier transform
RCA	right coronary artery
SAX	short axis
SSFP	steady state free precession
2CH	2-chamber